Development of Numerical Circular Wave Basin and Investigation of Tsunami-Structure Interaction

REN Xingyue

Supervised by

Prof. MIZUTANI Norimi

Costal and Ocean Engineering Laboratory

Department of Civil Engineering

Nagoya University

Japan

Acknowledgements

I would like to offer my sincerest gratitude to my supervisor, Prof. Mizutani Norimi, who has supported me throughout this research with his patience and knowledge, allowing me the room in my own way. Without him, this thesis would not have been written or completed. I am heartily thankful to Assoc. Prof. Kawasaki Koji and Assoc. Prof. Nakamura Tomoaki for their knowledgeable advices in seminars, and Assoc. Prof. Nakamura Tomoaki for the helpful suggestions in discussions.

I would like to express sincere thanks to the dissertation committee, which consists of Prof. Mizutani Norimi (Head), Prof. Tsujimoto Tetsuro, Prof. Saitoh Takehisa from Kanazawa University, Assoc. Prof. Kawasaki Koji, Assoc. Prof. Toda Yuji, and Assoc. Prof. Nakamura Tomoaki for the careful review and valuable suggestions on this work.

I also extend my thanks to Mr. Peng Wei, Mr. Manawasekara Chathura for the warm friendship and all the members of the Coastal Engineering Laboratory.

I am grateful to Prof. Shi Bing, the supervisor of my master course in Ocean University of China, and the members in his Laboratory for sending me papers published in academic journals in Chinese. And special appreciation goes to the Chinese Scholarship Council for the financial support.

Finally, I would like to express my deep sense of gratitude to my parents and sister for their loves and understandings.

ABSTRACT

Development of Numerical Circular Wave Basin and Investigation of Tsunami-Structure Interaction

Since marine structures are operated under the real conditions of the open sea, accurate prediction of waves plays a key role in solving coastal and ocean engineering problems, especially for pre-designing hydraulic responses of coastal and offshore structures. In numerical or physical wave basins, the real sea waves, which consist of multi-directional and oblique waves, are generally generated by the snake-movement of the serpent wave generator according to the wave maker theory. There are two factors affecting the effective area of the reproduced wave field in the practical application of the multi-directional and oblique wave generations in three-dimensional wave basins, which are wave reflections and wave diffractions, for the re-reflected waves from wave generation paddles and side walls of the basin disturb the wave field after certain time of simulation and wave diffraction makes the generated wave be not able to preserve its energy.

To reproduce the multi-directional and oblique waves with larger effective test area, a numerical circular wave tank model is developed based on the two-phase incompressible flow model by solving the Navier-Stokes equations in cylindrical coordinates and tracking the free surface with the volume of fluid (VOF) method. Oblique waves are generated with a transparent wave generator, and the outgoing waves are numerically dissipated in a dumping zone at the outer edge of the wave basin. In this model, the finite volume method (FVM) is used to discretize the control equations over the zonal embedded grid system that is implemented to overcome the

stability issue in the cylindrical coordinates. The computational components are stored according to the staggered grid arrangement. Velocities and pressure are coupled with the projection method. To solve the VOF convection equation over the zonal embedded grids, an algebraic CICSAM-VOF method is applied, which is proposed to track the free surface over unstructured grids. Validations of the two-phase incompressible flow model are carried out with the circular dam breaking problems in a circular basin and good agreements can be found from the computational results.

Oblique waves are successfully reproduced in the proposed circular wave basin. Comparisons of the numerical results with analytical results shows that this model can reliably reproduce oblique waves with enlarged effective area. This model is extended to multi-directional wave simulations by integrating the mass wave source of oblique waves. Two crossing waves are carried out as a case study in this thesis. As a result, the circular wave basin is numerically built for the generation of oblique and multi-directional waves.

Tsunami-bridge interaction is carried out based on numerical and experimental studies. The characteristic of wave forces acting on the bridge and the relationship between the bridge failure and wave forces are discussed. Usage of the developed circular wave basin to Tsunami-Bridge interaction will be carried out by applying unstructured grids to model a rectangular bridge in cylindrical coordinates.

Keywords: Circular wave basin; Numerical simulation; Navier-Stokes Equations; Tsunami-bridge interaction.

Table of Contents

Chapter 1

Introduction

1.1 Study background and motivation

Waves, mainly generated by wind in the deep sea, transport to the coastal region where their height will increase during this process, change the topography at the shallow water region near the coastal region and act on costal structures. In the open seas and coastal area, ships, marine and coastal structures are periodically confronted to severe complex nonlinear directional waves from time to time, and those structures are also facing huge extreme waves and tsunami, which constitute major problems for both the structure integrity and human safety. The tsunami caused by the great east Japan earthquake in March 11, 2011, took 15883 deaths, 6145 injured, and 2671 people missing, as well as 129225 buildings totally collapsed, with a further 254204 buildings 'half collapsed', and another 691766 buildings partially damaged. The tsunami also caused extensive and severe structural damage, including heavy damage to coastal structures, roads, railways and bridges. It is necessary to investigate the characteristics of interaction of ocean waves, including tsunami, and structure to help the coastal and offshore designers giving suitable design solutions in order to meet both the safe and economical requirements. Therefore, an increasing number of dedicated test facilities

have been built for that purpose in the past decades. Based on experimental studies, Burcharth et al. (2006) analyzed the structural stability of detached low crested breakwaters under irregular waves, and Hsiao and Lin (2010) simulated the tsunami waves overtopping and impinging a seawall with solitary waves.

The regular, irregular and solitary waves reproduced with two-dimensional section wave tanks in laboratory have been mature and reliable approached by researchers and engineers to test coastal and offshore structure models, and the main challenge is on the simulation of the real sea waves, the three-dimensional waves that are quite random in propagating directions as well as amplitudes and periods. Three-dimensional waves can be reproduced in three-dimensional wave basins shown in Fig. 1-1 with the separate wave generator installed along one or more side boundaries of the wave basin. However, it is well known that the issue that how to enlarge the effective wave area is the fundamental topics for three-dimensional wave basin models, where the ineffective dissipation of the wave reflections from side walls, wave generator paddles and experimental structures and the wave diffractions will deform the wave field after certain time.

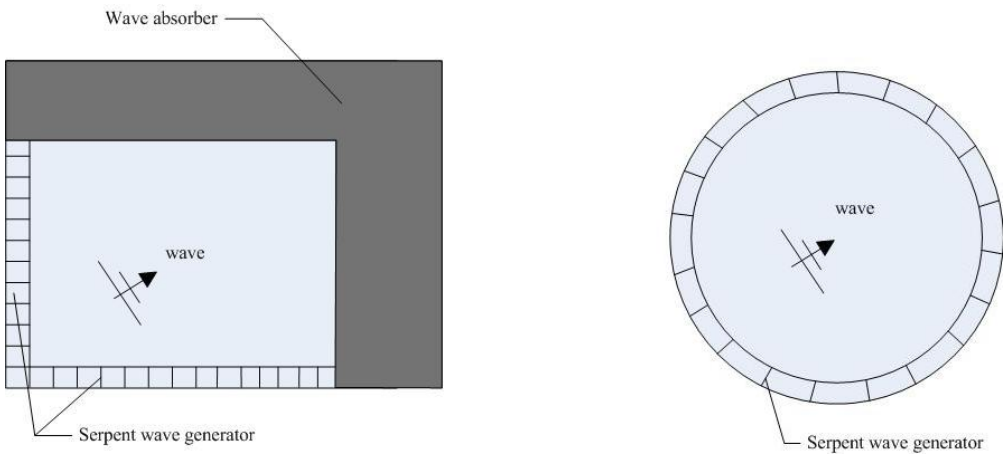

Fig. 1-1. Three-dimensional wave basins with serpent wave generator.

Left: rectangular wave basin;

Right: circular wave basin.

To enlarge the effective experimental area, Funke and Miles (1987) using the corner reflector and Dalrymple (1989) with side wall reflection practically increased the effective area in the three-dimensional wave basin for the reproductions of oblique waves. Hiraishi et al. (1995) successfully reproduced the multi-directional waves according to a directional wave spectrum, and the effective area is also significantly enlarged with multi-face wave generator, although the effective area is affected by the incident angle of waves in the wave basin. On the other hand, Tanaka et al. (1994) proposed a concept of the three-dimensional wave basin that waves can be generated in any direction in a circular wave basin without affecting the performance of the wave basin. Based on this concept that waves are generated by a transparent wave generator inside the wave basin and both reflected waves from experimental models and outgoing waves are dissipated by the dumping zone located at the outer boundary of the basin, both numerical studies with the boundary element based potential theory model and experimental studies in laboratory were carried out. In their paper, comparisons with traditional rectangular basin showed the perfect performances of this circular wave basin in the application to the oblique wave generations and that the effect of the incident angle to the effective area can be neglected in this wave basin. Naito (2006) also built a circular wave basin shown in the right panel of Fig. 1-1, which is capable to generate small amplitude waves. Plan waves are generated by the absorbing wave maker arranged in a circle at the outer boundary of the basin based on the combination of cylindrical waves so that the wave generation method is more complicated than that in the circular basin proposed by Tanaka et al. (1994), where waves are generated by a transparent wave source method.

The circular wave basin can enlarge the effective area of the oblique wave field and the effect to the effective area of the wave incident angle can be neglected in the circular wave basin (Tanaka et al., 1994), which is advanced in reproduction of oblique waves. Therefore, the present thesis is motivated to develop a numerical circular wave basin that can generate oblique waves and apply this wave basin to

study wave-structure interactions, as the main characteristic of waves in the real sea is the wave direction and waves normally approach to the offshore and coastal structures, and shorelines at an oblique angle.

1.2 Development of numerical wave tanks

Since the high cost and technical limitations of the experimental facilities limit the utilizations of laboratory experiments with wave flumes or wave basins and the available computational power has increased to be able to treat larger computations, numerical wave tanks that use a computer code to achieve the final goals to reproduce physical wave tanks as closely as possible have been developed as an alternative for experimental investigations of wave involved problems for decades. In the recent years, various numerical wave tanks have been widely applied to investigate the wave involved problems. Two main approaches to the numerical wave tanks are categorized as models based on inviscid and irrotational flows and models based on viscous flows. In the first category, the Laplace equation and nonlinear free surface conditions are solved usually using the boundary element method (BEM). In the latter category, the unsteady Navier-Stokes equations are solved for simulating the exact fluid movements.

1.2.1 Potential theory based models

Numerical solvers based on the potential theory for wave simulations assumed the flow as inviscid, incompressible and irrotational idea flow solve the velocity potential controlled by Laplace equation normally with the boundary element method (BEM). Ohyama and Nadaoka (1991) proposed a two-dimensional wave flume model for analyzing nonlinear and irregular waves. In that model, waves were generated with a wave source method and outgoing waves were dissipated in a dumping zone. Using boundary element method (BEM), Williams and Crull (2000) proposed a three-dimensional wave basin based on the potential theory for oblique waves

generated by the serpent wave generator, and analyzed the performance of the model with waves of different incident angles. In their study, the effective area in the rectangular wave basin was analyzed to be related to the wave reflection and wave diffraction, which is affected by the wave incident angle. Simulation of Oblique waves and vertical cylinder was carried out and the influence of the cylinder on the wave field was presented in their study. Shih et al. (2009), with multi-face wave generator, reproduced the oblique and multi-directional waves in a rectangular wave basin based on the three-dimensional boundary element potential theory models.

1.2.2 Navier-Stokes solvers based models

Numerical waves can be reproduced in numerical wave tanks as an application of the incompressible interfacial flow models by solving the Navier-Stokes equations. Two types of incompressible interfacial flow model, the single-phase and the two-phase model, categorized by whether the air phase is considered or not, have been applied in the last decades. In the single-phase flow model, the computational domain filled by air phase is not considered so that the free surface should be treated as a boundary, where pressure is computed by the linear interpolation. While in the two-phase fluid model, the whole domain is computed based on the reformulated control equations where the free surface is treated as a smoothed or sharp region.

Using the single-phase flow model, Nichols et al. (1980) proposed the SOLA-VOF model with the volume of fluid (VOF) method to track the free surface. Austin and Schlueter (1982) presented the first application of SOLA-VOF code to predict waves in a porous armor layer of a rectangular block breakwater. Iwata et al. (1996) analyzed wave breaking phenomenon due to the submerged structure by modifying the SOLA-VOF method with a wave source method proposed by Brorsen and Larsen (1987). Lin and Liu (1998) incorporated a $\kappa - \varepsilon$ Reynolds-averaged Navier-Stokes (RANS) turbulence model in the Ripple code (Kothe et al., 1991), the developed vision of SOLA-VOF code, and then investigated the turbulence generated by

breaking waves on a sloping bottom. However, RANS models are usually too dissipative for the simulation of highly unsteady breaking waves. On the other hand, using large-eddy simulation of turbulence, Christensen and Deigaard (2001) studied the characteristics of the turbulent flow of breaking waves with SOLA-VOF code.

Using the two-phase fluid model, the detailed information of the free surface can be calculated. Lubin et al (2006) proposed a three-dimensional large-eddy simulation of air entrainment under the plunging breaking waves using the computational fluid dynamic library Aquilon developed in the TREFLE laboratory. Hieu et al. (2004), with SMAC method to solve the Naiver-Stokes equation, volume of fluid method to track the free surface, built a two-phase model for the investigation of breaking waves.

All those numerical models above are used to simulate two-dimensional waves, and Park et al. (2003, 2004) proposed a numerical wave model using the incompressible Navier-Stokes solver for the simulation of multi-directional waves with marker-density function method to treat the fully nonlinear kinematic free surface condition. Application to wave and vertical cylinder interaction with this model is also presented in their papers. Similar work was also carried out by Chio and Yoon (2009) with the commercial Computational Fluid Dynamic (CFD) tool, Fluent, where oblique waves were generated by the wave source method.

1.3 Study objectives

As discussed above, the circular wave basin can practically improve the technique of the oblique and multi-directional wave generation and all the studies are based on the rectangular ones in the field of numerical wave tanks based on Navier-stokes solvers. Therefore, it is necessary to develop a circular wave basin based on the incompressible two-phase incompressible flow model governed by Navier-Stokes equations, since only the inviscid and irrotational flow model for the circular wave basin was considered in the previous studies. The specific contents of this thesis are as

follows,

1) Develop a numerical circular wave basin and apply it to oblique wave-structure interactions;
2) Apply the proposed numerical model to the analyze tsunami-bridge interaction.
3) Experimental studies and numerical studies of the tsunami-bridge interaction in section wave tank are presented in this thesis.

1.4 Thesis outline

Based on the two-phase incompressible flow model, a numerical circular wave basin which is capable of reproducing oblique waves with the wave source method is proposed in the present study. The content of this thesis is organized as follows,

In Chapter 2, a three-dimensional two-phase incompressible flow model in cylindrical coordinates is developed. In this model, the projection method is used to solve the Navier-Stokes equations over zonal embedded grids which are used to generate a smoothed grid system in the entire computational domain to avoid that too small time steps should be used in the computation. The free surface is tracked by the volume of fluid (VOF) method and the free surface tension is also considered with the Continuum Surface Force (CSF) method in this study. Two cases that a volume of water breaks inside the cylindrical tank have been used to validate the two phase model.

In Chapter 3, experimental and numerical studies on the tsunami and bridge interaction are carried out to analyze the bridge failures by evaluating tsunami forces acting on the bridge, since the recent events, the Indian Ocean tsunami in 2004 and the great East Japan tsunami in 2011, have brought the importance of investigation of bridge failures induced by tsunami.

In Chapter 4, the numerical circular wave basin is developed and applied to the investigation of oblique waves based on the two-phase incompressible flow model proposed in Chapter 2. Oblique waves are generated with a transparent wave source

method first implemented by Larsen and Dancy (1983) and the outgoing waves are numerically dissipated by the artificial dumping zone. Based on this model, the interaction of oblique waves with a vertical cylinder is discussed.

Finally, the main conclusions and the intension for the future researches are presented in Chapter 5.

References:

Austin, D. I. and Schlueter, R. S., 1982. A numerical model of wave breaking breakwater interactions. Proceeding of the 18th International Conference on Coastal Engineering, Vol. 3, Cape Town, Republic of South Africa, pp.2079-2096.

Burcharth, H. F., Kramer, M., Lamberti, A. and Zanuttigh, B., 2006. Structural stability of detached low crested breakwaters, Coastal Engineering 53, 381-394.

Choi, J. and Yoon, S. B., 2009. Numerical simulations using momentum source wave-maker applied to RNS equation model. Coastal Engineering 56, 1043-1060.

Christensen, E. D. and Deigaard, R., 2001. Large eddy simulation of breaking waves. Coastal Engineering 41, 53-86.

Christensen, E. D., Walstra, D.-J. and Emerat, N., 2002. Vertical variation of the flow across the surf zone. Coastal engineering 45, 169-198.

Dean, R. G. and Dalrymple, R. A., 1984. Water wave mechanics for scientists and engineerings. Prentice-Hall, Englewood Cliffs, NJ.

Dalrympe, R. A., 1989. Directional wavemaker theory with sidewall reflection. Journal of Hydraulic Research. 27, 23-34

Funke, E. R., Miles, M. D., 1987. Multi-directional wave generation with corner reflectors. Technical report No. TR-HY-021, National research council hydraulic lab., Ottawa, Canada.

Hieu, P. D., Katsutoshi, T., and Ca, V. T., 2004. Numerical simulation of breaking waves using a two-phase flow model. Applied Mathematical Modelling 28, 983-1005.

Hiraishi, T., Kanazawa, T. and Fujisaku, H., 1995. Development of multi-face directional random wave maker. Proceeding of 5th International Offshore and Polar Engineering conference (ISOP), Hague, Netherlands.

Hsiao, S. C. and Lin T. C., 2010. Tsunami-like solitary waves impinging and overtopping an impermeable seawall: experiment and RANS modeling, Coastal Engineering 57, 1-18.

Ito, K., Katsui, H., Mochizuki, M. and Isobe, M., 1996. Non-reflected multi directional wave maker theory and experiments of verification. Proceeding of 25th International Conference of Coastal Engineering(ICCE), Orlando, Florida.

Iwata, K., Kawasaki, K. and Kim, D.-S., 1996. Breaking limit, breaking and post-breaking wave deformation due to submerged structures. Proceeding of the 25th International Conference on Coastal Engineering, Vol. 3, Orlando, USA, pp.2338-2351.

Kawasaki, K., 1999. Numerical simulation of breaking and post-breaking wave deformation process around a submerged breakwater. Coastal Engineering Journal 41, 201-223.

Kothe, D. B., and Mjolsness, R. C., 1991. REPPLE: A computer program for incompressible flows with interfaces. Report LA-12007-MS, Los Alamos, CA, USA.

Larsen, J. and Dancy, H., 1983. Open boundaries in short waves simulation: a new approach. Coastal Engineering 7, 285-297.

Lin, P. Z. and Liu, P. L.-F., 1998. A numerical study of breaking waves in surf zone. Journal of Fluid Mechanics 359, 239-264.

Lin, P. Z. and Liu, P. L.-F., 1999. Internal wave-maker for Navier-Stokes equations models. Journal of Water, Port, Coastal and Ocean Engineering 125, 207-215.

Lubin, P., Vincent, S., Abadie, S. and Caltagirone, J.-P., 2006. Three-dimensional large-eddy simulation of air entrainment under plunging breaking waves. Coastal Engineering 53, 631-655.

Naito, S., 2006. Wave generation and absorption – theory and application. Proceeding of 16th international offshore and polar engineering conference (ISOP), San Fracisco, California, USA.

Nichols, B. D., Hirt, C. W. and Hotchkiss, R. S., 1980. SOLA-VOF: a solution algorithm for transient fluid flow with multiple free boundaries. Report LA-8355, Los Alamos, CA, USA.

Park, J. C., Kim, M. H., Miyata, H. and Chun, H.-H., 2003. Fully nonlinear numerical wave tank (NWT) simulations and wave run-up prediction around 3-D structures. Ocean Engineering 30, 1969-1996.

Park, J. C., Uno, Y., Sato, T., Miyata, H. and Chun, H.-H., 2004. Numerical reproduction of fully nonlinear multi-directional waves by a viscous 3D numerical tank. Ocean Engineering 31,1549-1565.

Shih, R.-s., Chou, C.-R. and Weng, W.-K., 2009. Numerical modelling of 3D oblique waves by L-type multiple directional wave generator. Proceeding of 19th International Offshore and Polar Engineering Conference, Osaka, Japan.

Tanaka, M., Ohyama, T., Kiyokawa, T. and Nadaoka, K., 1994. Non-reflective multi-directional wave generation by source method. Proceedings of 24th Conference on Coastal Engineering, Kobe, Japan.

Williams, A. N. and Crull, W. W., 2000. Simulation of directional waves in a numerical basin by a desingularized integral equation approach. Ocean engineering **27**, 603-624.

Chapter 2

Two-phase incompressible flow model in cylindrical coordinates

2.1 Mathematical models

For two incompressible, immiscible fluids that are separated by a moving surface, the motion of both fluids can be described by the Navier-Stokes equations. Since the discontinuities in physical properties such as density, viscosity at the interface can be treated in different ways, the governing equations can be reformulated into two types: the single fluid model which treats two fluids as a single fluid using a transition region across the interface and the jump condition model which treats the free surface sharply.

In this section, a mathematical representation of two immiscible flows, each having a constant viscosity, is presented, and this mathematical model includes the surface tension. With the single-fluid assumption, the whole domain considered can be divided into two sub-domains which are occupied by different fluids and marked by a step color function, which is one in one particular fluid and zero elsewhere. Hence, the density as well as other material property can be written in terms of their constant values on either side of the interface and the color function. At the interface, the discontinuous properties, such as density, viscosity and surface tension are needed to be smoothed over a transition region of the finite thickness.

2.1.1 Control equations of single-fluid model formulation

The fluid motion is assumed to be governed by the Navier-Stokes equations for an impressible fluid. Based on the single-fluid assumption, the control equations have to account both the differences of the material properties as well as the surface tension acting on the interface. Thus, the continuity and momentum equations can be written as

$$\nabla \cdot \vec{\mathrm{U}} = 0 \ , \tag{2-1}$$

$$\frac{\partial \vec{U}}{\partial t} + \nabla \bullet (\vec{U}\vec{U}) = -\frac{1}{\rho}\nabla P - \vec{g} + \frac{1}{\rho}\nabla \bullet \vec{\tau} + \frac{1}{\rho}\overrightarrow{F_b}, \tag{2-2}$$

where $\vec{U}$ is the velocity, ρ the density, P the pressure, $\vec{\tau}$ the viscous stress tensor, $\vec{g}$ the gravity acceleration and $\overrightarrow{F_b}$ the body force due to the surface tension.

The density and viscosity are interpolated with a weight factor calculated from the color function as

$$\rho = \rho_W H + \rho_A (1 - H), \tag{2-3}$$

$$\mu = \mu_W H + \mu_A (1 - H), \tag{2-4}$$

where subscripts W and A denote water and air respectively. The weight factor H is the smoothed color functions differencing both the two fluids and the free surface transition region (the volume fraction is used in the present model).

2.1.2 Interface simulation method

Numbers of techniques used to track the free surface have been developed in the last four decades. Two main approaches are available for the free surface flow simulation: interface tracking and interface capturing methods (Ferziger and Peric, 1996). In the first categories, the interface is represented by attaching it to the mesh boundary which is forced to move with the free surface. In the second category, the fluids on either side of the interface are represented by either massless particles or indicator functions. Interface tracking methods are Lagrangian kind method, employing a computational mesh that moves with the interface, while the interface

capturing methods, on the other hand, use a Eulerain mesh fixed in space, where the position and movement of the free surface is captured by the solution algorithm itself. The most widely used schemes of the surface capturing method are the maker and cell (MAC) method (Harlow and Welch, 1965), the level set (LS) method (Osher and Sethian, 1988) and volume of fluid (VOF) method (Hirt and Nichols, 1981).

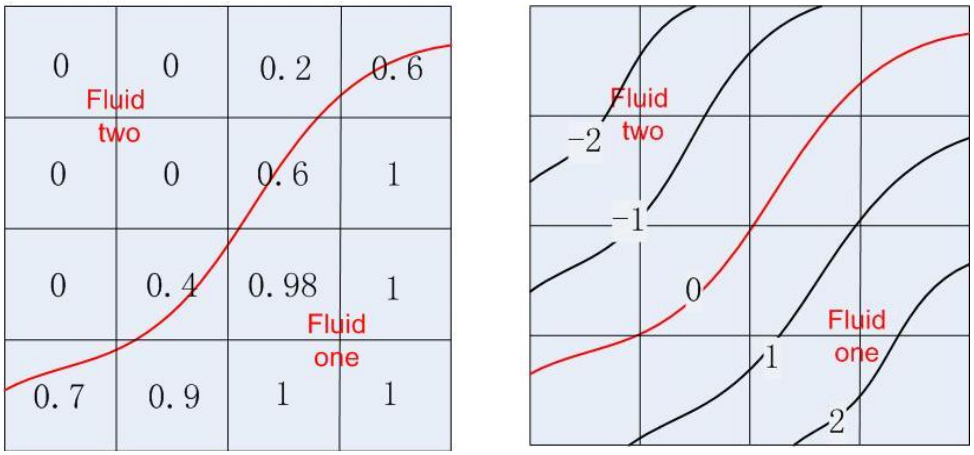

Fig. 2-1. Illustrations of VOF and Level set method.

Left: volume fraction for VOF method;

Right: distance function for Level set method.

With the MAC method, the massless particles are introduced in the domain filled with water, and then the particles are tracked using a simple Lagrangian movement equation. The level set method introduces a scalar function defined to be the minimum distance to the interface. Thus, the interface can be captured to be where the scalar has a value of zero (Fig. 2-1).

VOF method, one of the most widely used interface capturing algorithms, is first proposed by Hirt and Nichols (1981). With the VOF method, a scalar indicator function F between 1 and 0 (Fig. 2-1), defined as a volume fraction, is used to distinguish between two fluids and the interface is not treated as a sharp boundary but a transition region exists where the fluid is treated as the mixture of the two fluids.

The volume fraction function is defined as:

- $F = 1$ control cells filled only with fluid one，
- $F = 0$ control cells filled only with fluid two，
- $0 < F < 1$ interfacial cells，

where F is the volume fraction. It is associated with each fluid and is hence propagated with fluids as a Lagranginan invariant (Hirt and Nichols, 1981). Therefore, it obeys a transport equation of the form:

$$\frac{\partial F}{\partial t} + (\nabla \bullet \vec{U})F = 0. \tag{2-5}$$

To solve this equation without numerical artificial diffusion or dispersion, two types of methods are introduced in the recent three decades: geometrical interface-reconstructing methods and methods based on algebraically formulated differencing schemes. The geometric methods, consisting of several methods such as Simple Line Interface Calculation (SLIC) method, Piecewise Linear Interface Calculation (PLIC), Youngs's method and so on (reviewed by Scardoveli and Aaleski, 1999), reconstruct the free surface with pricewise lines and then calculate the convection equation based on those reconstructions. These methods are mainly used for two-dimensional free surfaces capturing over the rectangular grid system because of the complexities of the free surface re-construction. On the other hand, the algebraic methods are easier to implement, some of these methods are possible to apply to the computation over unstructured grids. With the cell face flux computed by a high order and a low order scheme, Zalesak (1979) proposed the flux corrected transport algorithm to predict the convection equation with a limitor to avoid numerical diffusion. Xiao (2005) developed a one dimensional algebraic interface capture method based on the tangent function and Yokoi (2007) extended this method to multi-dimensional interfacial flows computation using a weighting factor computed from the surface normal. Based on the high resolution scheme, Ubbind et al. (1999) proposed the most popular CICSAM scheme for the free surface flow simulation over the unstructured meshes.

2.1.3 Surface tension model

Within a fluid with interfaces, the cohesive forces are unbalanced due to the discontinuity of fluid properties at the interface and that result in the surface tension effect. With the single-fluid assumption, the surface tension, only affecting at the interface, is a part of the source term in momentum equations.

Brackbill et al. (1992) proposed a CSF (continuum surface force) model which use a smoothed body force acted as the surface tension within the transition region and affiliate the body force to the Navier-Stokes equation as a source term directly. With this model the body force is calculated from

$$\overrightarrow{F_b} = \sigma\kappa(\vec{n})\vec{n}\delta \,, \tag{2-6}$$

where σ is the coefficient of the surface tension, κ the mean curvature, $\vec{n}$ the normal to the surface and δ a delta function which is only nonzero at the transition region.

2.2 Projection method

Since there is no known analytical solution of the Navier-Stokes and continuity equations, they must be solved numerically. Using the explicit scheme to approximate the time derivative, the momentum equation with respect to time can be written as:

$$\frac{\overrightarrow{U^{n+1}} - \overrightarrow{U^n}}{\Delta t} = -\nabla \bullet (\overrightarrow{U^n}\overrightarrow{U^n}) - \frac{1}{\rho^n}\nabla P^{n+1} - \vec{g} + \frac{1}{\rho^n}\nabla \bullet \overrightarrow{\tau^n} + \frac{1}{\rho^n}\overrightarrow{F_b^{\,n}} \,, \tag{2-7}$$

where n means the previous time step and $n+1$ means the calculation time step.

The most common methods to solve Eq. (2-7) are the Projection methods and the SIMPLE-like methods. The projection method is first introduced by Chorin (1968) based on the theory of Helmholtz-Hodge decomposition, and it is getting increasing popular in application to the simulation of viscous incompressible flows. With the projection method, one first finds an approximation of the velocity and then projects the approximated velocities into a divergence field, the velocity field, and a scalar

field, the pressure field based on the Helmholtz-Hodge decomposition.

To find the approximated velocity, named as intermediate or tentative velocity in other papers, one needs to solve the equation:

$$\frac{\overrightarrow{U^*}-\overrightarrow{U^n}}{\Delta t}=-\nabla\bullet(\overrightarrow{U^n}\overrightarrow{U^n})-\frac{1}{\rho^n}\nabla P^n-\vec{g}+\frac{1}{\rho^n}\nabla\bullet\overrightarrow{\tau^n}+\frac{1}{\rho^n}\overrightarrow{F_b^{\,n}}\,. \tag{2-8}$$

To ensure the continuity Eq. (2-1), one needs to project the approximated velocity into a divergence-free vector. Submitting Eq. (2-8) to Eq. (2-7), one can get

$$\frac{\overrightarrow{U^{n+1}}-\overrightarrow{U^*}}{\Delta t}=-\frac{1}{\rho^n}\nabla(P^{n+1}-P^n)\xrightarrow{P^{'}=P^{n+1}-P^n}\overrightarrow{U^{n+1}}=\overrightarrow{U^*}-\frac{\Delta t}{\rho^n}\nabla(P^{'})\,. \tag{2-9}$$

Take the divergence in both sides of Eq. (2-9), in a result, the pressure Poisson equation is formulated by applying the continuity equation, as:

$$\frac{1}{\Delta t}\nabla\bullet\overrightarrow{U^*}=\nabla\bullet(\frac{1}{\rho^n}\nabla(P^{'}))\,. \tag{2-10}$$

Since P' is calculated from Eq. (2-10), velocities and pressure can be corrected with Eq. (2-9). Therefore, all the variables of the control equation are calculated by the above equations.

2.3 Control equations in cylindrical coordinates

In cylindrical coordinates, the continuous Eq. (2-1) is written as

$$\frac{1}{r}\frac{\partial ru}{\partial r}+\frac{1}{r}\frac{\partial v}{\partial\theta}+\frac{\partial w}{\partial z}=0\,, \tag{2-11}$$

where u is the velocity component in the radial direction, v the velocity component in the azimuthal direction and w the velocity component in the vertical direction.

Since the turbulence model is not considered in this study, the Navier-Stokes equations, Eq. (2-2), lead to

$$\begin{aligned}&\frac{\partial u}{\partial t}+u\frac{\partial u}{\partial r}+\frac{v}{r}\frac{\partial u}{\partial\theta}+w\frac{\partial u}{\partial z}-\frac{v^2}{r}=\\&-\frac{1}{\rho}\frac{\partial p}{\partial r}+\frac{\partial}{r\partial r}(\nu\frac{\partial ru}{\partial r})+\frac{\partial}{r^2\partial\theta}(\nu\frac{\partial u}{\partial\theta})+\frac{\partial}{\partial z}(\nu\frac{\partial u}{\partial z})-\frac{\nu u}{r^2}-\frac{2\nu}{r^2}\frac{\partial v}{\partial\theta}+\frac{1}{\rho}F_r\end{aligned}\,, \tag{2-12}$$

$$\frac{\partial v}{\partial t}+u\frac{\partial v}{\partial r}+\frac{v}{r}\frac{\partial v}{\partial \theta}+w\frac{\partial v}{\partial z}-\frac{uv}{r}=$$
$$-\frac{1}{r\rho}\frac{\partial p}{\partial \theta}+\frac{\partial}{r\partial r}(\nu\frac{\partial rv}{\partial r})+\frac{\partial}{r^2\partial \theta}(\nu\frac{\partial v}{\partial \theta})+\frac{\partial}{\partial z}(\nu\frac{\partial v}{\partial z})-\frac{\nu v}{r^2}-\frac{2\nu}{r^2}\frac{\partial u}{\partial \theta}+\frac{1}{\rho}F_\theta, \tag{2-13}$$

$$\frac{\partial w}{\partial t}+u\frac{\partial w}{\partial r}+\frac{v}{r}\frac{\partial w}{\partial \theta}+w\frac{\partial w}{\partial z}=$$
$$-\frac{1}{\rho}\frac{\partial p}{\partial z}-g+\frac{\partial}{r\partial r}(\nu\frac{\partial rw}{\partial r})+\frac{\partial}{r^2\partial \theta}(\nu\frac{\partial w}{\partial \theta})+\frac{\partial}{\partial z}(\nu\frac{\partial w}{\partial z})+\frac{1}{\rho}F_z. \tag{2-14}$$

Table 2-1: Values of ϕ and S_ϕ for the general form equation in a cylindrical coordinates.

Momentum equation in	ϕ	S_ϕ
r direction	u	$-\frac{1}{\rho}\frac{\partial p}{\partial r}-\frac{\upsilon}{r}(\frac{2}{r}\frac{\partial v}{\partial \theta}+\frac{u}{r})+\frac{v^2}{r}+\frac{1}{\rho}F_r$
θ direction	v	$-\frac{1}{\rho}\frac{1}{r}\frac{\partial p}{\partial \theta}+\frac{\upsilon}{r}(\frac{2}{r}\frac{\partial u}{\partial \theta}-\frac{v}{r})-\frac{uv}{r}+\frac{1}{\rho}F_\theta$
z direction	w	$-\frac{1}{\rho}\frac{\partial p}{\partial z}-g+\frac{1}{\rho}F_z$

Before the discretization, the momentum equations can be written into the form of the convection and diffusion equation in cylindrical coordinates, which is known as the general form of control equations and widely used in the finite volume method. The general form of the control equations (He et al., 2004, Xue, 1999) is

$$\frac{\partial(\phi)}{\partial t}(unsteady\ term)+\nabla\bullet(\vec{U}\phi)(convection\ term)$$
$$=\nabla\bullet\left(\nu\nabla\phi\right)(diffusion\ term)+S_\phi(source\ term), \tag{2-15}$$

or

$$\frac{\partial(\phi)}{\partial t}(unsteady\ term)+\left(\frac{1}{r}\frac{\partial(u\phi)}{\partial r}+\frac{1}{r}\frac{\partial(v\phi)}{\partial\theta}+\frac{\partial(w\phi)}{\partial z}\right)(convection\ term)=$$
$$\left(\frac{1}{r}\frac{\partial}{\partial r}(\upsilon r\frac{\partial\phi}{\partial r})+\frac{1}{r}\frac{\partial}{\partial\theta}(\frac{\upsilon}{r}\frac{\partial\phi}{\partial\theta})+\frac{\partial}{\partial z}(\upsilon\frac{\partial\phi}{\partial z})\right)(diffusion\ term)+S_{\phi}(source\ term)\ .$$

(2-16)

The contents of the coefficients and the source terms for different dependent variables are summarized in Table 2-1.

2.4 Discretization with finite volume method

The continuous problem must be reduced to the discrete problem so that a computer can digest it. There are mainly three kinds of discretization method: the Finite Difference Method (FDM), the Finite Volume Method (FVM) and the Finite Element Method (FEM). In this section, Discretization of the control equations is based on the finite volume method.

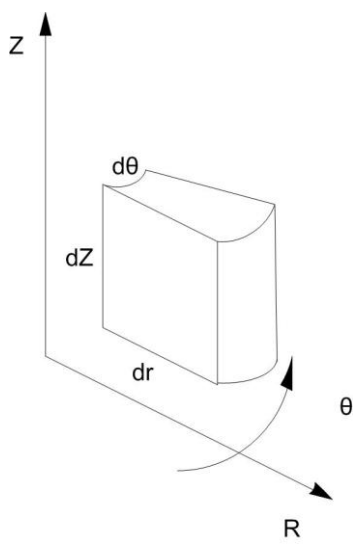

Fig. 2-2. Control volume in cylindrical coordinate system.

The entire computational domain is first divided into a set of non-overlapping control volumes, also known as grids, which can be regular or irregular in size and

shape. With the finite volume method, integrate the equations over the control volumes and then the control equations can be transformed into the discretized form from the continuous form.

In this thesis, zonal embedded grids are used to discretize the control equation.

2.4.1 Zonal embedded grid method

Use of the numerical method in cylindrical coordinates also reveals a fundamental problem when the regular rectangular grid system is employed (Fig. 2-3). As it is well known, under the regular grid system extremely small time steps must be taken for the sake of numerical stability, when an explicit method is employed, for the grid size at the outer boundary is usually ten or hundred times greater than that near the axis, especially, when the diameter of the cylindrical computational domain is very large. In this thesis, the circular wave basin for the simulations of three-dimensional waves, which is the target of this thesis, is a cylindrical tank with a diameter times of the height so that the regular rectangular grid system is not suitable for this model.

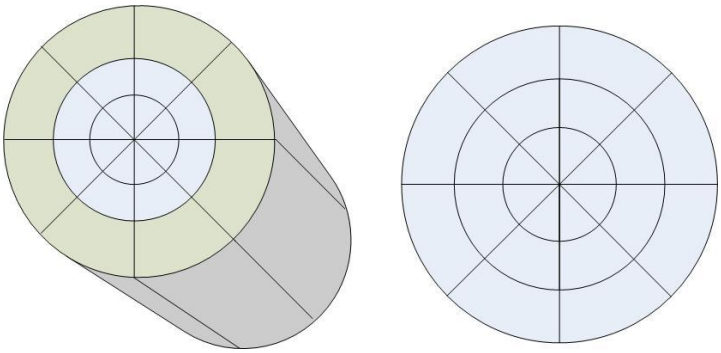

Fig. 2-3. Rectangular grid system in cylindrical coordinates.

Herein the zonal embedded grid system shown in Fig. 2-4 rather than the regular rectangular grid system is implemented. With the zonal embedded grid method, the entire computational domain is divided into many blocks, and in every block, the grid

generation is as the same way as that with the regular rectangular grid generation method. Fig. 2-4 shows the zonal embedded grid system that the computational domain is divided into two blocks and the regular rectangular grids are generated in every block.

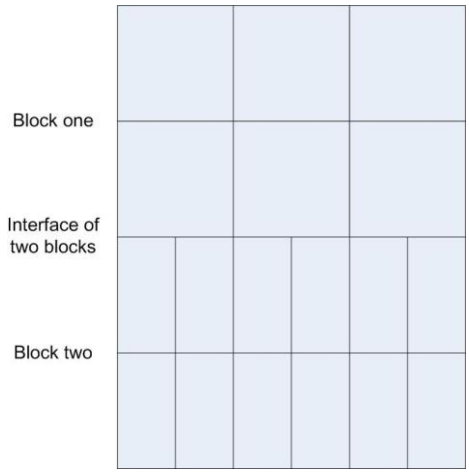

Fig. 2-4. Zonal embedded grid system.

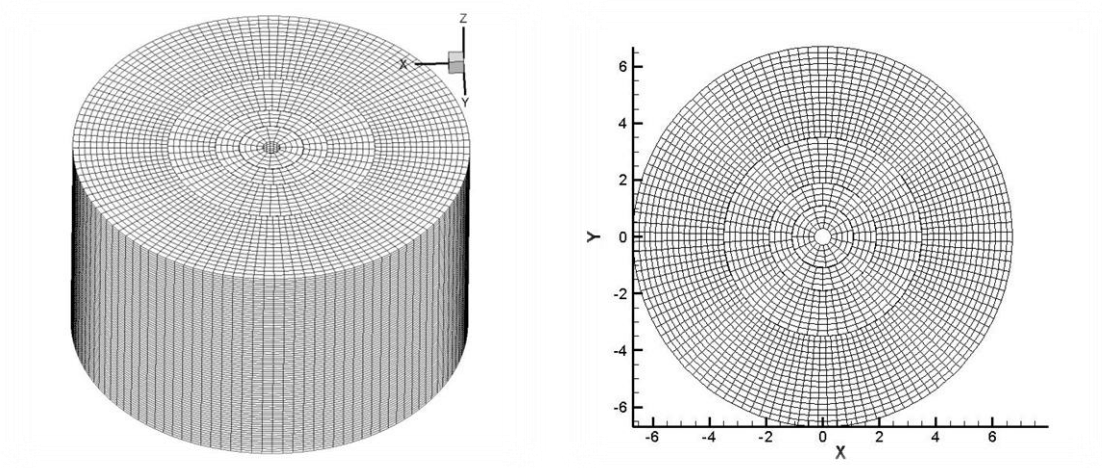

Fig. 2-5. Zonal embedded grids in cylindrical coordinates.

In the present study, the computational domain is divided into many concentric cylinders along the radial direction and the grid number in each block can be

determined based on the method proposed by Suh and Yeo (2006) in polar coordinates. For a computational domain that is separated into M blocks, I_M, the number of radial grids, J_M, the number of azimuthal grids and K_M, the number of vertical grids in each block, are given by

$$\begin{aligned} \mathrm{I}_M &= \begin{cases} I_0 & for\ M = 1 \\ 2^{M-2} I_0 & for\ M >= 2 \end{cases} \\ J_M &= 2^{M-1} J_0 \\ K_M &= K_0 \end{aligned} \quad , \tag{2-17}$$

where I_0, J_0 and K_0 are the number of grids in the first zone. A four-block zonal embedded grid system used for the dam breaking case study is shown in Fig. 2-5.

2.4.2 Staggered grid

Harlow and Welch (1965) introduced the staggered arrangement that offers several advantages over the collocated arrangement. This arrangement is shown in Fig. 2-6, where the velocities and pressure are stored in different locations. Take the cell (i, j, k) as a example, the pressure P and some other scalar variables such as density, viscosity and volume fraction are put in the centre of the cell indexed as (i, j, k) and velocities are stored in cell faces indexed as $(i \pm 1/2, j \pm 1/2, k \pm 1/2)$.

As mentioned in Section 2.2, velocities and pressure are coupled with the projection method in the computational domain and the biggest advantage of the staggered arrangement is the strong coupling between the velocities and the pressure. With the staggered arrangement, the continuity equation that requires interpolation with the collocated arrangement can be calculated directly. This helps to avoid some types of convergence problems and oscillations in pressure and velocities fields.

Since the zonal embedded grids method has been applied, the geometry of the control cells at the interface between two blocks (Fig 2-6) is different with that of the normal ones. Therefore, special treatments are need in the computation of the variables at these control cells, which will be discussed in the next sections.

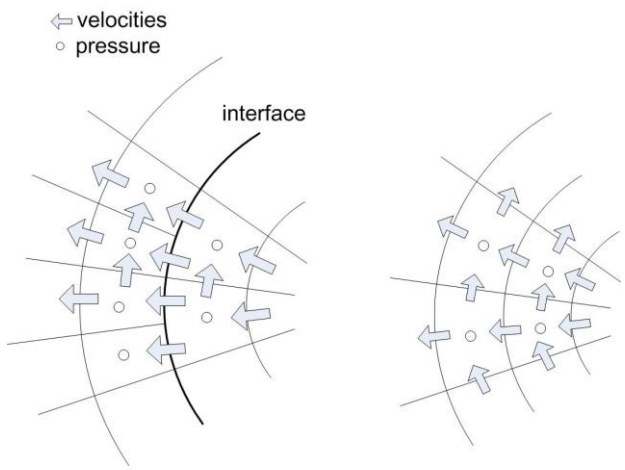

Fig. 2-6. staggered grid.

Left: arrangement of the interfacial control cells

Right: arrangement of the normal control cells

2.4.3 Navier-Stokes euqations computation

The discretized equation is derived by integrating the general form equation, Eq. (2-16), over control volumes and the time interval from t to $t + \Delta t$. Thus,

$$\int_{\Delta t}\int_{\Delta v} \frac{\partial(\phi)}{\partial t} dtdv + \int_{\Delta t}\int_{\Delta v} \nabla \bullet (\vec{U}\phi) dtdv = \int_{\Delta t}\int_{\Delta v} \nabla \bullet (\nu \nabla \phi) dtdv + \int_{\Delta t}\int_{\Delta v} S_{\phi} dtdv , \tag{2-18}$$

where Δt and Δv are the time step and volume of the control volume. Using the Gauss theory, the integration over the control volume can be explained by the integration over the faces of the control volume, and then the Eq. (2-18) can be written as:

$$\int \frac{\partial \phi}{\partial t} \Delta v dt = \int \sum_{Nf} \nu \nabla \phi_f \vec{n} \Delta s dt - \int \sum_{Nf} \vec{U} \phi_f \vec{n} \Delta s dt + \int S_{\phi} \Delta v dt . \tag{2-19}$$

And the continuity equation can be discretized with the same method,

$$\sum_{Nf} \vec{U} \vec{n} \Delta s = 0 . \tag{2-20}$$

Then the governing equations have been disctrtized over the control volumes and time internal by the finite volume method.

Assumptions, like explicit, Crank-Nicolson (C-N) and fully implicit schemes are possible to approximate the convection, diffusion and source terms from the time t to time $t+\Delta t$. In the current study, to make the coding easier, the explicit scheme is applied and approximation within a time step is computed with the second-order Admas-Bashforth (AB) scheme. Based on the time assumption scheme, the approximated velocity with the projection method can be calculated with the discretized formula:

$$\frac{(\phi^* - \phi^n)}{\Delta t}\Delta v = 2(\sum_{Nf} \nu \nabla \phi_f \vec{n}\Delta s - \sum_{Nf} \vec{U}\phi_f \vec{n}\Delta s)^n - (\sum_{Nf} \nu \nabla \phi_f \vec{n}\Delta s - \sum_{Nf} \vec{U}\phi_f \vec{n}\Delta s)^{n-1} + S_\phi \Delta v$$

. (2-21)

Compute all the approximated components of the momentum equations summarized in Table 2-1, and project the approximated velocities into the convergence free field, the corrective pressure equation is discretized as:

$$\frac{\Delta t}{\rho^n}\sum_{Nf} \nabla P' \vec{n}\Delta s = \sum_{Nf} \overrightarrow{U^*}\vec{n}\Delta s \,. \tag{2-22}$$

Using Eq. (2-9), the velocities can be computed with the corrective pressure.

2.4.3.1 Approximation of convection term

The computation of the convection term is the major cause of numerical difficulties: the central difference scheme leads to unphysical oscillatory behaviors in regions of flow where the convection donates the diffusion, and thereby violating the boundedness of the solution; the classical first order upwind scheme overcomes those difficulties, but it increasingly imparts errors, so-called numerical diffusion.

In order to reduce the unphysical numerical oscillations and, at the same time, minimize the effects of the artificial diffusion, a number of high order convection schemes, including the composite schemes, have been developed over the past years, Using the combination of high order schemes and the first order upwind scheme and blending them together by the limiters such as Total Variation Diminishing (TVD) and

Normalized Variable Diagram (NVD), the composite schemes have been developed to avoid the numerical diffusion of the upwind method and unboundedness of the high order schemes, such as the QUICK scheme and the second order upwind scheme. In this thesis, the NVD based high resolution scheme is used to compute the face variable.

The convection term in Eq. (2-21) is calculated by integrating the velocity flux over the control cell. The velocity flux is a multiply of the flux velocity $\vec{U}\vec{n}$, variable at cell faces ϕ_f and the face area. The flux velocity is usually computed by the central interpolation and the face variable ϕ_f is calculated by the high resolution SMART schemes in the present study. Then the discretized convection term can be written as:

$$\sum_{Nf}\vec{U}\phi_f\vec{n}\Delta s = \frac{u_{i-1,j,k}+u_{i,j,k}}{2}\phi_{f,w}\Delta s_w + \frac{u_{i+1,j,k}+u_{i,j,k}}{2}\phi_{f,e}\Delta s_e \frac{v_{i+1,j,k}+v_{i,j,k}}{2}\phi_{f,s}\Delta s_s + \frac{v_{i+1,j+1,k}+v_{i,j+1,k}}{2}\phi_{f,n}\Delta s_n + \frac{w_{i+1,j,k}+w_{i,j,k}}{2}\phi_{f,b}\Delta s_b + \frac{w_{i+1,j,k+1}+w_{i,j,k+1}}{2}\phi_{f,t}\Delta s_t, \tag{2-23}$$

where the subtitles w, e, s, n, b, t means the west, east, south, north, bottom and top faces of the control cell. As mentioned above, in the application of the zonal embedded grids, the discretization over the control cells at the interfaces are different with the regular ones, because both the velocities at fine and coarse blocks are needed for the flux velocities interpolation and the face variables computation with the SMART scheme. The discretized convection term over the control volumes at the interface can be rewritten as

$$\sum_{Nf}\vec{U}\phi_f\vec{n}\Delta s = \frac{u_{i-1,j,k}+u_{i,j,k}}{2}\phi_{f,w}\Delta s_w + \frac{u_{fine\ block}+u_{i,j,k}}{2}\phi_{f,es}\Delta s_{es} + \frac{u_{fine\ block}+u_{i,j,k}}{2}\phi_{f,en}\Delta s_{en} + \frac{v_{i+1,j,k},v_{i,j,k}}{2}\phi_{f,s}\Delta s_s + \frac{v_{i+1,j+1,k},v_{i,j+1,k}}{2}\phi_{f,n}\Delta s_n + \frac{w_{i+1,j,k},w_{i,j,k}}{2}\phi_{f,b}\Delta s_b, + \frac{w_{i+1,j,k+1},w_{i,j,k+1}}{2}\phi_{f,t}\Delta s_t \tag{2-24}$$

where es and en donate the faces of the control volume at the interface. The

geometry of those control volumes is different with the regular cells, for there are two neighboring control volumes with which share the same faces es and en.

To compute the face variable ϕ_f with the high order SMART schemes, the local behavior of the convection variables near a control volume face for one dimensional uniform grids shown in Fig. 2-7, U, D, A, the node labels represent the upwind cell, donator cell and acceptor cell according to the convective velocity direction there and the velocity direction in this figure is assured greater than zero.

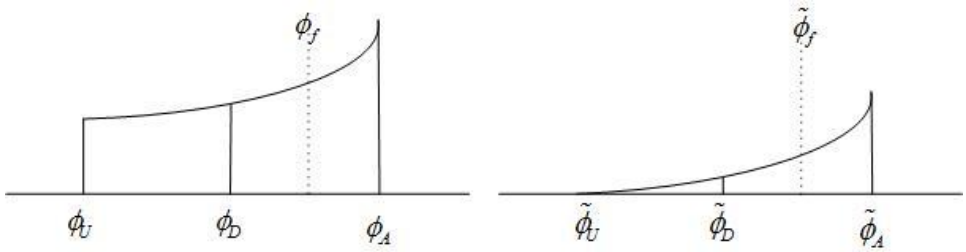

Fig. 2-7. Definition of variables.

One can determine the value of the face variable with the interpolation explained by $\phi_f = F(\phi_U, \phi_D, \phi_A)$. This value is affected by all the values in the three neighboring nodes. Leonard (1991), normalizing the variable with the variables at the upwind and accepter nodes in uniform girds, proposed the normalized variables defined by $\tilde{\phi} = (\phi - \phi_U)/(\phi_A - \phi_U)$, and then the effect of the variables at the upwind and accepter nodes can be eliminated, and the profile to determine the normalized face variable is $\tilde{\phi}_f = \tilde{F}(\tilde{\phi}_D)$, which means the normalized face variable can be determined by the normalized variable at the donor cell. In this way, the third order QUICK scheme in uniform grids can be written with the formula $\tilde{\phi}_f = (6\tilde{\phi}_D + 3)/8$.

As mentioned earlier, high resolution schemes need a criterion to blend two or three different profiles with the boundedness upwind scheme to avoid unphysical numerical oscillations. Gaskell and Lau (1988) proposed a convection boundedness

criterion (CBC) for the one-dimensional implicit flow calculations and it has been widely used to construct the high order differencing schemes with the Normalize variable diagram (NVD) method. The CBC uses the normalized variable and stipulates the bounds of $\tilde{\phi}_f$ for which an implicit difference scheme always preserves the local boundedness criteria in one dimension:

$$\begin{aligned} &\tilde{\phi}_f = \tilde{\phi}_D \quad for\ \tilde{\phi}_D < 0\ or\ \tilde{\phi}_D > 1 \\ &0 < \tilde{\phi}_f < 1 \quad for\ \ 0 < \tilde{\phi}_D < 1 \end{aligned} \quad . \tag{2-25}$$

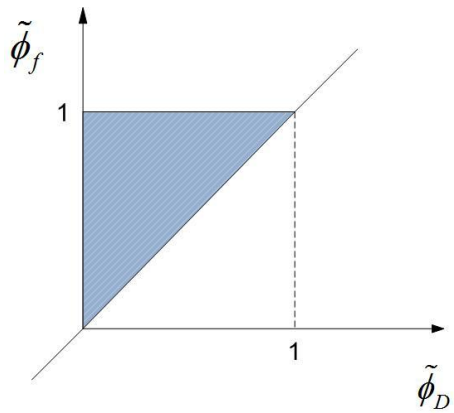

Fig. 2-8. NVD plots for CBC.

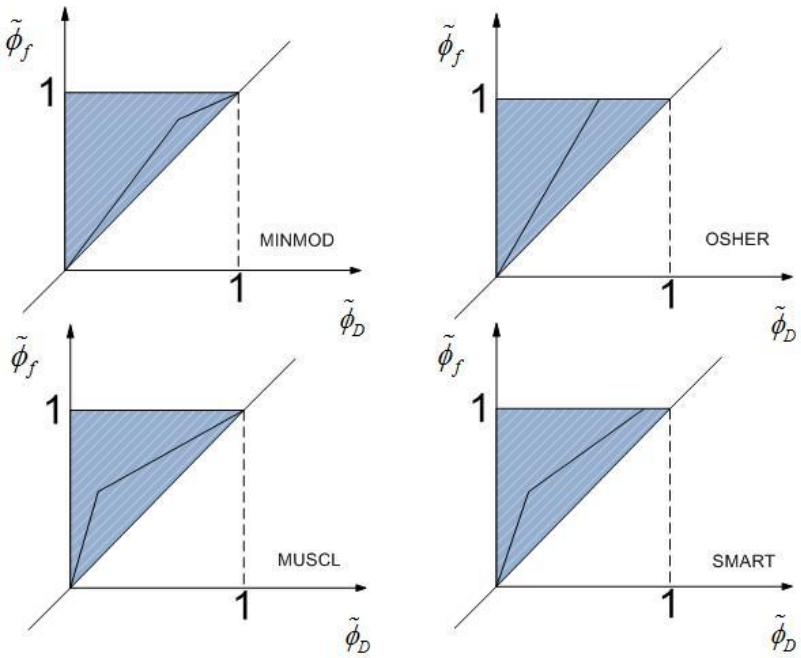

Fig. 2-9. NVD plots for various high resolution schemes.

Table 2-2. Functional relationships for high resolution schemes (uniform grid) (Darwish et al., 1996).

MINMOD	$\tilde{\phi}_f = \begin{cases} \frac{3}{2}\tilde{\phi}_D & 0 < \tilde{\phi}_D < \frac{1}{2} \\ \frac{1}{2}\tilde{\phi}_D + \frac{1}{2} & \frac{1}{2} \le \tilde{\phi}_D < 1 \\ \tilde{\phi}_D & elsewhere \end{cases}$
OSHER	$\tilde{\phi}_f = \begin{cases} \frac{3}{2}\tilde{\phi}_D & 0 < \tilde{\phi}_D < \frac{2}{3} \\ 1 & \frac{2}{3} \le \tilde{\phi}_D < 1 \\ \tilde{\phi}_D & elsewhere \end{cases}$
MUSCL	$\tilde{\phi}_f = \begin{cases} 2\tilde{\phi}_D & 0 < \tilde{\phi}_D < \frac{1}{4} \\ \tilde{\phi}_D + 1 & \frac{1}{4} \le \tilde{\phi}_D < \frac{3}{4} \\ 1 & \frac{3}{4} \le \tilde{\phi}_D < 1 \\ \tilde{\phi}_D & elsewhere \end{cases}$
SMART	$\tilde{\phi}_f = \begin{cases} 3\tilde{\phi}_D & 0 < \tilde{\phi}_D < \frac{1}{6} \\ \frac{3}{4}\tilde{\phi}_D + \frac{1}{4} & \frac{1}{6} \le \tilde{\phi}_D < \frac{5}{6} \\ 1 & \frac{5}{6} \le \tilde{\phi}_D < 1 \\ \tilde{\phi}_D & elsewhere \end{cases}$

Fig. 2-8 shows the normalized variable diagram (NVD) with CBC, which plots the normalized variable at the cell face as a function of the normalized variable of the donor cell and the shaded area in this figure is the reasonable area that confirm the bound. High order differencing schemes with a value outside the shaped area is the scheme out of boundedness. Using CBC, researchers usually construct the high resolution scheme by blending parts of the high order schemes inside the shaded area and the first order upwind scheme. Based on this approach, a number of preserving high resolution methods were formulated (Table 2-2) and Fig 2-9 shows the profiles

of those high resolution schemes in NVD (Darwish et al., 1996). In this thesis, SMART method is used to compute the face variable ϕ_f.

2.4.3.2 Approximation of diffusion term

To calculate the diffusion term, the central deference scheme is used for the calculation of the velocity gradient. The discretized diffusion term in Eq. (2-21) can be written as:

$$\begin{aligned}\sum_{Nf} \nu \nabla \phi \vec{n} \Delta s = {} & \nu_s \frac{(\phi_{i,j,k} - \phi_{i-1,j,k})}{\Delta r} \Delta s_w + \nu_e \frac{(\phi_{i+1,j,k} - \phi_{i,j,k})}{\Delta r} \Delta s_e \\ & + \nu_s \frac{(\phi_{i,j,k} - \phi_{i,j-1,k})}{r_{i-1/2} \Delta \theta} \Delta s_s + \nu_n \frac{(\phi_{i,j+1,k} - \phi_{i,j,k})}{r_{i-1/2} \Delta \theta} \Delta s_n \,, \\ & + \nu_b \frac{(\phi_{i,j,k} - u_{i,j,k-1})}{\Delta z} \Delta s_b + \nu_t \frac{(\phi_{i,j,k+1} + \phi_{i,j,k})}{\Delta z} \Delta s_t\end{aligned} \tag{2-26}$$

where the subtitles w, e, s, n, b, t means the west, east, south, north, bottom and top faces of the control cell and for the control volumes at the interface, the discretized diffusion term is formulated as:

$$\begin{aligned}\sum_{Nf} \nu \nabla \phi \vec{n} \Delta s = {} & \nu_w \frac{(\phi_{i,j,k} - \phi_{i-1,j,k})}{\Delta r} \Delta s_w \\ & + \nu_{es} \frac{(\phi_{fine\,block} - \phi_{i,j,k})}{\Delta r} \Delta s_{es} + \nu_{en} \frac{(\phi_{fine\,block} - \phi_{i,j,k})}{\Delta r} \Delta s_{en} \\ & + \nu_s \frac{(\phi_{i,j,k} - \phi_{i,j-1,k})}{r_{i-1/2} \Delta \theta} \Delta s_s + \nu_n \frac{(\phi_{i,j+1,k} - \phi_{i,j,k})}{r_{i-1/2} \Delta \theta} \Delta s_n \\ & + \nu_b \frac{(\phi_{i,j,k} - u_{i,j,k-1})}{\Delta z} \Delta s_b + \nu_t \frac{(\phi_{i,j,k+1} + \phi_{i,j,k})}{\Delta z} \Delta s_t\end{aligned} \,, \tag{2-27}$$

where the velocities $\phi_{fine\,block}$ are linearly interpolated from the neighboring nodes.

The viscosity in Eqs. (2-26) and (2-27) is computed by the interpolation of the values in the vertexes of the control cell, which are computed from the centre values of all the neighboring cells by:

$$\begin{aligned}\nu_{i-1/2,j-1/2,k-1/2} = {} & (\nu_{i-1,j-1,k-1} + \nu_{i-1,j,k-1} + \nu_{i-1,j-1,k} + \nu_{i-1,j,k} \\ & + \nu_{i,j-1,k-1} + \nu_{i,j,k-1} + \nu_{i,j-1,k} + \nu_{i,j,k}) / 8\end{aligned} \,, \tag{2-28}$$

and the density is computed with the same method.

2.4.3.3 Source term and Poisson equation

The difference term in the source term like $\partial v/\partial\theta$ for the momentum equations are computed using the central difference. The most important issue for the source term is the computation of the pressure gradient that is also used for the Poisson equation computation, which is approximated with a central difference in the present study. As the zonal embedded grid method is implemented, at the interface cells (Fig. 2-10), special interpolation schemes are needed to construct the central difference for the cells at the interface.

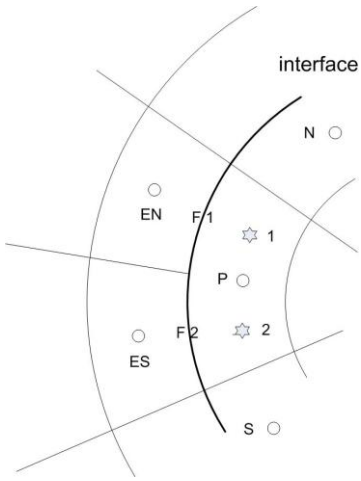

Fig 2-10. Discretization of pressure gradient.

To compute the pressure gradient with the central difference scheme at the faces $F1$ and $F2$ shown in Fig. 2-10, one needs the values of the variables at the nodes *1* and *2*, and these can be interpolated from the nodes N, P and S. Lasasso et al. (2004, 2006), without any interpolations, substituted the value at node P to construct the central difference at the faces *F1* and *F2*. In their model, the velocities at these two faces are same. While in this thesis, a second accuracy result is achieved with the following interpolation equation (Popinet, 2003),

$$\begin{aligned} P_1 &= \frac{15}{16}P_P - \frac{3}{32}P_S + \frac{5}{32}P_N \\ P_2 &= \frac{15}{16}P_P - \frac{3}{32}P_N + \frac{5}{32}P_S \end{aligned} \quad . \tag{2-29}$$

All the pressure gradient terms, both in the Poisson equation and correction equation, are computed with the central difference scheme based on these interpolations.

There are three types of control cells in the zonal embedded grids: the normal type, control volumes that are neighboring with a fine block and control volumes that are neighboring with a coarse block. The discretized form of the Poisson equation can be written as, for regular cells:

$$\begin{aligned} & A_pP_P + A_wP_w + A_eP_e + A_sP_s + A_nP_n + A_bP_b + A_tP_t = rhs \\ & A_p = -(A_w + A_e + A_s + A_n + A_b + A_t) \\ & A_w = \Delta s_w / \Delta r / \rho_w \\ & A_e = \Delta s_e / \Delta r / \rho_e \\ & A_s = \Delta s_s / r_s \Delta\theta / \rho_s \\ & A_n = \Delta s_n / r_n \Delta\theta / \rho_n \\ & A_b = \Delta s_b / \Delta z / \rho_b \\ & A_t = \Delta s_t / \Delta r / \rho_t \\ & rhs = (u_e\Delta s_e - u_w\Delta s_w + u_n\Delta s_n - u_s\Delta s_s + u_t\Delta s_t - u_b\Delta s_b) / \Delta t \end{aligned} \quad , \tag{2-30}$$

where A is the coefficient and the subtitles donate the faces of the control volume as the same as last section. For the second type, (the cell P in Fig. 2-10), the discretization of the Poisson equation can be written as:

$$\begin{aligned} & A_pP_P + A_wP_w + A_{es}P_{es} + A_{en}P_{en} + A_sP_s + A_nP_n + A_bP_b + A_tP_t = rhs \\ & A_p = -(A_w + A_{es} + A_{en} + A_s + A_n + A_b + A_t) \\ & A_{en} = \Delta s_{es} / \Delta r / \rho_{es} \\ & A_{en} = \Delta s_{en} / \Delta r / \rho_{en} \\ & A_s = \Delta s_s / r_s \Delta\theta / \rho_s + \frac{3}{32}A_{en} - \frac{5}{32}A_{es} \\ & A_n = \Delta s_n / r_n \Delta\theta / \rho_n + \frac{3}{32}A_{es} - \frac{5}{32}A_{en} \\ & rhs = (u_{es}\Delta s_{es} + u_{en}\Delta s_{en} - u_w\Delta s_w + u_n\Delta s_n - u_s\Delta s_s + u_t\Delta s_t - u_b\Delta s_b) / \Delta t \end{aligned} \quad . \tag{2-31}$$

And for the last type (the cell es or en in Fig. 2-10) the Poisson equation is

discretized as:

$$
\begin{aligned}
&A_p P_P + A_w P_w + A_{ws} P_{ws} + A_{ws} P_{ws} + A_e P_e + A_s P_s + A_n P_n + A_b P_b + A_t P_t = rhs \\
&A_p = -(A_w + A_{wn} + A_{ws} + A_e + A_s + A_n + A_b + A_t) \\
&tem = \Delta s_w / \Delta r / \rho_w \\
&A_w = \frac{15}{16} tem \\
&A_{ws} = \frac{5}{32} tem \ \ or \ -\frac{3}{32} tem \\
&A_{wn} = -\frac{3}{32} tem \ \ or \ \frac{5}{32} tem \\
&rhs = (u_e \Delta s_e - u_w \Delta s_w + u_n \Delta s_n - u_s \Delta s_s + u_t \Delta s_t - u_b \Delta s_b) / \Delta t
\end{aligned}
\quad , \qquad (2\text{-}32)
$$

With Eqs. (2-30), (2-31) and (2-32) over all the control volumes, one can get the linear equations of the Possion equation, and these linear equations should be computed with suitable linear solvers. That will be discussed in the next section.

2.4.4 Treatment of singularity at the cylindrical axis

On the discretization of the governing equations at the axis, terms like $1/r$ or $\partial\phi/\partial r$ become undefined causing a singularity at the cylindrical centre, when the cylindrical centre is within the computational domain. In order to circumvent these difficulties, different numerical treatments for the definition of boundary conditions at the cylindrical axis have been proposed in literatures.

A method for dealing with this problem is to employ a mixed Cartesian and cylindrical grids system, which implements the Cartesian grids in the region near the axis and cylindrical grids where is away from the axis. That complexes the coding and some simplifications have been applied to compute the fluid flow quantities on the axis with extrapolations or averages. But these methods may cause a reduction in the overall computational accuracy. On the other hand, Verzicoo and Orlandi (1996) introduced special variables which are always 0 on the axial through reforming the control equations and de Davis (1979) suggested a discretization without nodes on the axis by adding a thin cylinder on the axis.

In the present study, following the idea of de Davis, with a small cylinder fixed in the axis, that problem can be treated as arbitrary boundary condition problems. It makes the coding easier and radial derivatives of innermost nodal points have been approximated by a second order forward finite difference formula.

2.4.5 Boundary conditions

Boundary conditions are imposed by setting the values of the nodes on the boundary and in the ghost cell directly. In this section, the west side boundary shown in Fig. 2-11 will be taken as an example.

2.4.5.1 No-slip condition

The continuous velocities should be zero at the boundary to satisfy the no-slip condition. The value of the cell lying directly on the boundary is set to equal to zero and for the value of cell not, the ghost cell method will be used.

2.4.5.2 Slip condition

In case of a slip condition, the velocity component normal to the boundary should be zero along with the normal derivative of the velocity component tangent to the boundary.

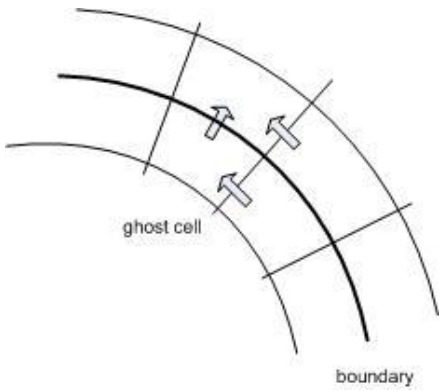

Fig. 2-11. Boundary condition.

2.4.5.3 Open boundary condition

In the open boundary condition the normal derivatives of both velocity components are set to zero at the boundary, which means that the total velocity does not change in the direction normal to the boundary.

2.4.6 Linear equation solver

As discussed in Section 2.4.3.3, with the zonal embedded grids, the cell numbering system is not ordered with the convenient identification on neighbor cells. Moreover the number of neighbor cells varies with the local grid configuration, which will make the coding for linear solver difficult. Hence, the set of linear equations forms a sparse matrix that is not the regular seven diagnoses matrix formed by the regular grid numbering system, which is solved using the Algebraic Multi Grid (AMG) method (Notay et al.), which is available on the personal website of Notay.

2.4.7 Time step restriction

In order to ensure stability of the numerical algorithm and avoid oscillations, stability condition must be imposed to restrict the time step.

The common used restriction condition is the Courant-Friedrichs-Lewy (CFL) condition which states that a fluid particle may not travel farther than one cell during one time step:

$$\begin{aligned} &|u\Delta t| < \Delta r \\ &|v\Delta t| < r\Delta\theta \\ &|w\Delta t| < \Delta z \end{aligned} \quad (2\text{-}33)$$

While in this model, a more series restriction condition that the time step should satisfy the cell courant number is less than 0.4, which is restricted by the stability of the volume of fluid method, is imposed.

2.5 Volume of fluid method

As discussed in the Section 2.1.2, the volume of fluid method employs the volume fraction as an indicator to mark different fluids. With the VOF method for the incompressible two-phase incompressible flow model, the convection equation for the indicator function is solved simultaneously with the continuity and momentum equations.

Discretization of the VOF convection equation has proven to be one of the most troublesome problems of the computational fluid dynamics (CFD) associated with the convection of the step function without diffusion, dispersing or wrinkling it. Researchers have proposed various techniques for capturing a well-defined interface based on an explicit Lagrangian convection of the reconstructed interface segments, which is difficult to be used in three-dimensional problems. An alternative to this problem is to discretize the VOF convection equation with differencing schemes that guarantee physical volume fraction values while preserve the smearing. Therefore, the high resolution differencing schemes such as the TVD based schemes, the Flux Corrected Transport (FCT) schemes and techniques based on the NVD method offer these options. Based on the NVD method, Ubbink and Issa (1999) proposed a surface-reconstructing free method named Compressive Interface Capturing Scheme for Arbitrary Mesh (CICSAM), which can be used in the unstructured grid system. In this study, the CICSAM method is extended to the zonal embedded grid system in cylindrical coordinates.

Using the method proposed by Ubbink and Issa (1999), the VOF convection equation is discretized with the finite volume method:

$$\begin{aligned}\frac{F^{n+1}-F^{n}}{\Delta t} &= -\frac{1}{\Delta v}\sum_{Nf}((\vec{U}F_f\vec{n}\Delta s)^{n+1}+(\vec{U}F_f\vec{n}\Delta s)^{n})/2 \\ &= -\frac{1}{\Delta v}\sum_{Nf}((fluxF_f)^{n+1}+(fluxF_f)^{n})/2\end{aligned}, \qquad (2\text{-}34)$$

where, $flux=\vec{U}\vec{n}\Delta s$, F_f is volume fraction face variable. The volume fraction values are solved simultaneously at the whole domain with the solution of the linear

equation from Eq. (2-34). The unphysical volume fraction values occurring from time to time cannot be neglected directly in this method as the method proposed by Hirt and Nichols (1981), since implicit method is used. To overcome this problem, Ubbink and Issa (1999) introduced a corrective procedure iterated with the approximation of the volume fraction by adjusting the weighting function that forms the coefficients of the linear equations. This process is time consuming and Heyns et al. (2013, 2011), proposed a Jacobi type dual-time stepping formulation approach instead of the approximation-corrector procedure, as:

$$\frac{F^{\tau+1}-F^{\tau}}{\Delta\tau}+\frac{F^{\tau}-F^{n}}{\Delta t}=-\frac{1}{\Delta v}\sum_{Nf}((fluxF_f)^{\tau+1}+(fluxF_f)^{n})/2, \tag{2-35}$$

the implicit solution will be approached as it convergence in the pseudo time τ.

2.5.1 CICSAM scheme

The face volume fraction can be calculated by the high resolution method with CICSAM method. CICSAM method is reconstructed based on the NVD schemes, which have been discussed in Section 2.4.3.

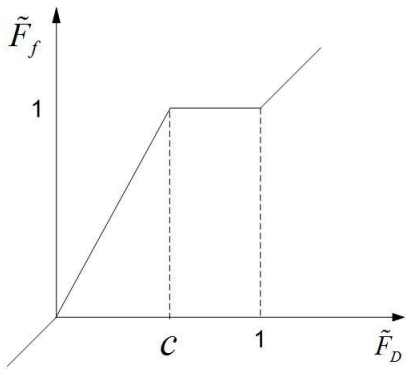

Fig. 2-12. NVD for Hyper-C scheme.

Fig. 2-8 shows the CBC criteria for one dimensional implicit flow calculation. It is too compressive to be used for the VOF convection equation computation. Ubbink

and Issa (1999), based on the study of Leonard (1991), using a linear weighting based on the cell Courant number c, constructed a suitable CBC criteria for the explicit flow calculation named as Hyper-C scheme, as:

$$\begin{aligned} &\tilde{F}_{f,cbc} = \tilde{F}_D && for\ \tilde{F}_D < 0\ or\ \tilde{F}_D > 1 \\ &0 < \tilde{F}_{f,cbc} < \min(1, \tilde{F}_D / c) && for\ \ 0 < \tilde{F}_D < 1 \end{aligned}, \tag{2-36}$$

where $\tilde{F}_D$, $\tilde{F}_f$ follow the definition in Section 2.4.3. This equation can be written in the actual volume fraction form:

$$\begin{aligned} &F_{f,cbc} = F_D && for\ r \le 1 \\ &F_{f,cbc} = \min(F_A, \frac{F_D - \tilde{F}_U}{c} + \tilde{F}_U) && for\ \ r > 1\ and\ F_D > \tilde{F}_U\ , \\ &F_{f,cbc} = \max(F_A, \frac{F_D - \tilde{F}_U}{c} + \tilde{F}_U) && for\ \ r > 1\ and\ F_D < \tilde{F}_U \end{aligned} \tag{2-37}$$

where $r = (F_A - \tilde{F}_U) / (F_D - \tilde{F}_U)$. In the multi-dimensional flow computation, the cell Courant number is defined as $c = \sum_{Nf} \left| c_{f,out} \right|$, where $c_{f,out}$ is the Courant number for each outflow face of the donor cell.

A differencing scheme which follows the CBC defined in Eq. (2-37) tends to compress any gradient into a step profile, and wrinkle the interface. To preserve the shape of the free surface interface, the CICSAM scheme blends the compressive Hyper-C scheme with the high resolution Ultimate-Quickest (UQ) scheme proposed by Leonard (1991), which reads

$$\begin{aligned} &\tilde{F}_{f,uq} = \tilde{F}_D && for\ \tilde{F}_D < 0\ or\ \tilde{F}_D > 1 \\ &0 < \tilde{F}_{f,uq} < \min(\tilde{F}_{f,cbc}, \frac{8c\tilde{F}_D + (1-c)(6\tilde{F}_D + 3)}{8}) && for\ \ 0 < \tilde{F}_D < 1 \end{aligned}. \tag{2-38}$$

This equation can also be extended to the actual volume form as:

$$\begin{aligned} &F_{f,uq} = F_D && for\ r \le 1 \\ &F_{f,uq} = \min(k, F_{f,cbc}) && for\ \ r > 1\ and\ F_D > \tilde{F}_U\ , \\ &F_{f,uq} = \max(k, F_{f,cbc}) && for\ \ r > 1\ and\ F_D < \tilde{F}_U \end{aligned} \tag{2-39}$$

where k defined by $k = F_U + (F_D - F_U)(3 + c) / 4 + 3(1 - c)(F_A - F_U) / 8$.

For the blending scheme, a key issue here is how to switch it between the Hyper-C

scheme and Ultimate-Quickest scheme. Hence a weighting factor γ between 0 and 1, based on the angle between the interface and the direction of the flow motion, is introduced for the prediction of the face variable,

$$\tilde{F}_f = \gamma \tilde{F}_{f,cbc} + (1-\gamma)\tilde{F}_{f,uq}, \tag{2-40}$$

And for the actual volume fraction,

$$F_f = \gamma F_{f,cbc} + (1-\gamma)F_{f,uq}. \tag{2-41}$$

Fig. 2-13 shows the CICSAM profile in different value of γ. The value $\gamma = 1$ is used when the interface orientation is normal to the direction of motion and $\gamma = 0$ when the interface is tangential to it. That implies that UQ operates when Hyper-C fails to preserve the gradient and Hyper-C operates when UQ fails to matins the sharpness of the interface.

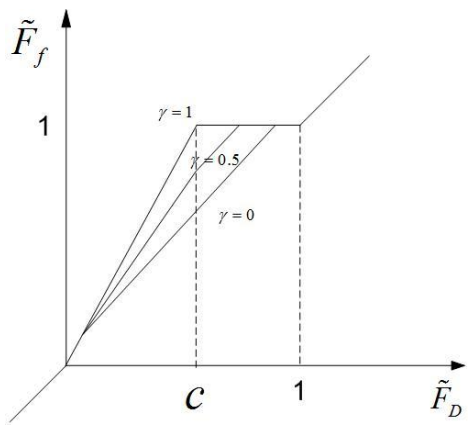

Fig. 2-13. NVD for CICSAM differencing scheme

The weighting factor suggested by Ubbind and Issa (1999) to blend the compressive and diffusive schemes is

$$\gamma = \min(k_\gamma \frac{\cos(2\theta_f)+1}{2}, 1), \tag{2-42}$$

where they recommend $k_\gamma = 1$ and

$$\theta_f = arc\cos\left|\frac{(\nabla F)_D \bullet \vec{d}}{\left|(\nabla F)_D\right|\left|\vec{d}\right|}\right|. \tag{2-43}$$

It is based on the cosine of the angle between the surface normal of donor cell and the distance vector connects the donor and acceptor cells.

With the CICSAM scheme to compute the volume fraction convection equation in multi-dimensional model, the cell Courant number limit is usually necessary to be less than $1/3$ (Gopala and van Wachem, 2008). That is much stricter than the Courant number limitation for the projection method discussed above.

2.5.2 Improvement to zonal embedded grids method in cylindrical coordinates

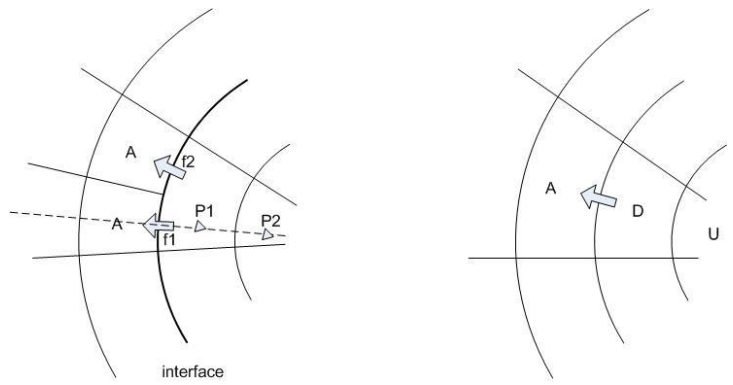

Fig. 2-14. Donor and acceptor cells.

Left: interface cells

Right: regular cells

In this study, a two-phase flow model is developed over the zonal embedded grids in cylindrical coordinates. Fig. 2-14 shows the interface cells and regular cells for the interpolation with CICSAM method over the embedded girds. When the face variable at face $f1$ is calculated, one needs the values at point $P1$ and $P2$ for donor and upwind cell values. Both of them are not located at the cell centre, thus, one need an

interpolation method to interpolate them from the cell centre. Jasak et al. (1999) overcome this problem with an interpolation from the donor cells based on the interface angle in unstructured grid systems. In this study, the cell face orientation is assumed parallel to the cell face inside a control volume, therefore interpolation is not needed but they are needed to be approximated to be the volume fraction value in the nearest cell.

2.6 surface tension model

As mentioned in Section 2.1.3, the Continuum Surface Force (CSF) model has been extensively used in the two-phase flow model coupled with VOF method since it was first introduced by Brackbill et al. (1992). In the CSF method, the discontinuous surface tension force is treated as a continuous body force distributed within a transition region of the finite thickness at the interface across which the fluid properties are assured to change continuously from one fluid to another.

2.6.1 Smoothing method

Several articles introduced what amounts in effect to distribute the surface tension over grid points in the transition region. The main differences in those articles are how to smooth the volume fraction and how to choose the delta function based on volume fraction values.

Brackbill et al. (1992) convolved the step volume fraction with a smooth kernel to construct a smoothed or mollified function and then calculated the surface normal and surface curvature based on the smoothed values. Lafaurie et al. (1994), to make the smooth process easily, used a regular mesh and define a Laplacian filter that transforms the volume fraction into a smoothed one. Both of the methods are proposed for regular mesh, and Ubbink (1997) implemented a smoothing method for unstructured mesh using a filter that is similar with that of Lafaurie et al. (1994). In the present model, the studies of Rusche (2002) is used to smooth the volume fraction

by means of elliptic relaxation,

$$\nabla \bullet (\frac{e}{|\vec{d}|} \nabla F^*) = F - F^* \quad , \tag{2-44}$$

where F^* is the smoothed volume fraction, $|\vec{d}|$ the vector between the centre of the cell of interest node and the centre of a neighbor cell and e is an adjustable coefficient related to the width of the transition region. Preliminary studies have shown that $e = 0.5$ gives good results.

After this smoothing operator, the surface normal vector is evaluated at the cell centre from the smoothed volume fraction. It is given by

$$\vec{n} = \nabla F^* . \tag{2-45}$$

The gradient is computed form

$$\nabla F^* = \frac{\sum_{nf} F_f^* \Delta s}{\Delta v} , \tag{2-46}$$

where Δv is the volume of the control cell and F_f^* is the face variable computed from the average of current cell and the neighbor cell that shares the face.

The CSF model demands a smoothed curvature value and it is calculated directly from the gradient of the smoothed volume fraction:

$$\kappa(\vec{n}) = -\frac{\nabla \bullet \vec{n}}{|\vec{n}|} = -\frac{1}{\Delta v} \sum_{nf} \frac{\nabla F_f^*}{|\nabla F_f^*|} \Delta s . \tag{2-47}$$

Following the study of Brackhill et al. (1992), the delta function chosen herein is the volume fraction gradient computed by Eq. (2-45)

2.7 Computational procedure

The finite volume discretization of the governing equations for the two-phase system in cylindrical coordinates has been presented. The free surface is tracked by the FVM based CICSAM-VOF method. The solution procedure for that two-phase fluid system over the embedded grids is:

1. Initialize all variables.

2. Calculate the Courant number (cell Courant number when the CICSAM-VOF method is used) and adjust the time step if it is necessary.

3. Solve new time velocity with the projection method.

4. Solve the volume fraction convection equation with the CICSAM-VOF method.

5. Save the data and return to step 2 until the end time.

The flow chart of the current two-phase model is presented in Fig. 2-15.

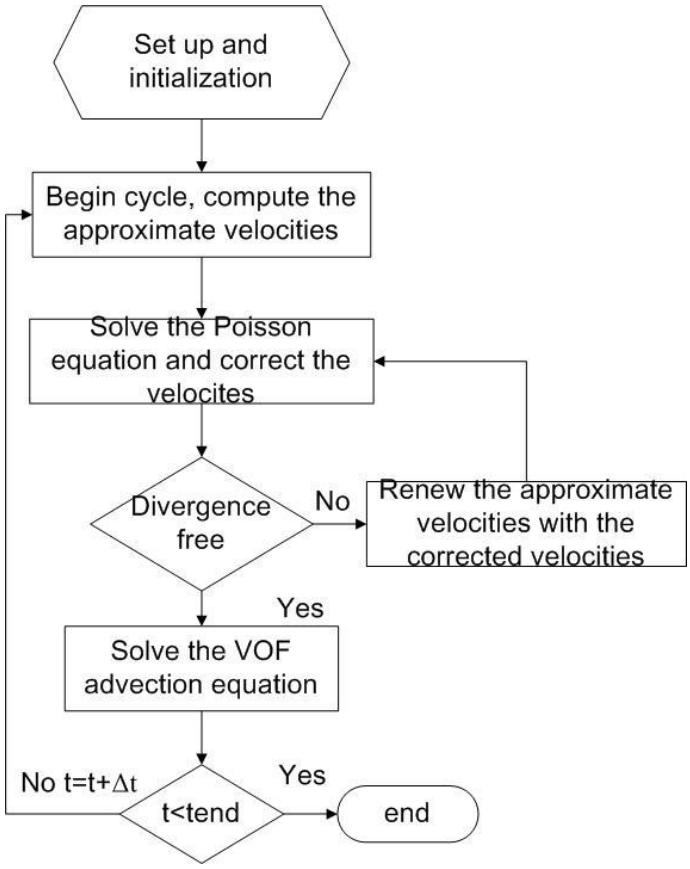

Fig. 2-15. Flow chart for computational cycle

2.8 Case studies

The Computational Fluid Dynamic (CFD) model for the incompressible two-phase flow motion has been built in the previous sections. In this section, to assess the performance of the present model to be applied to two-phase flow simulation, the

model will be tested using dam breaking problems.

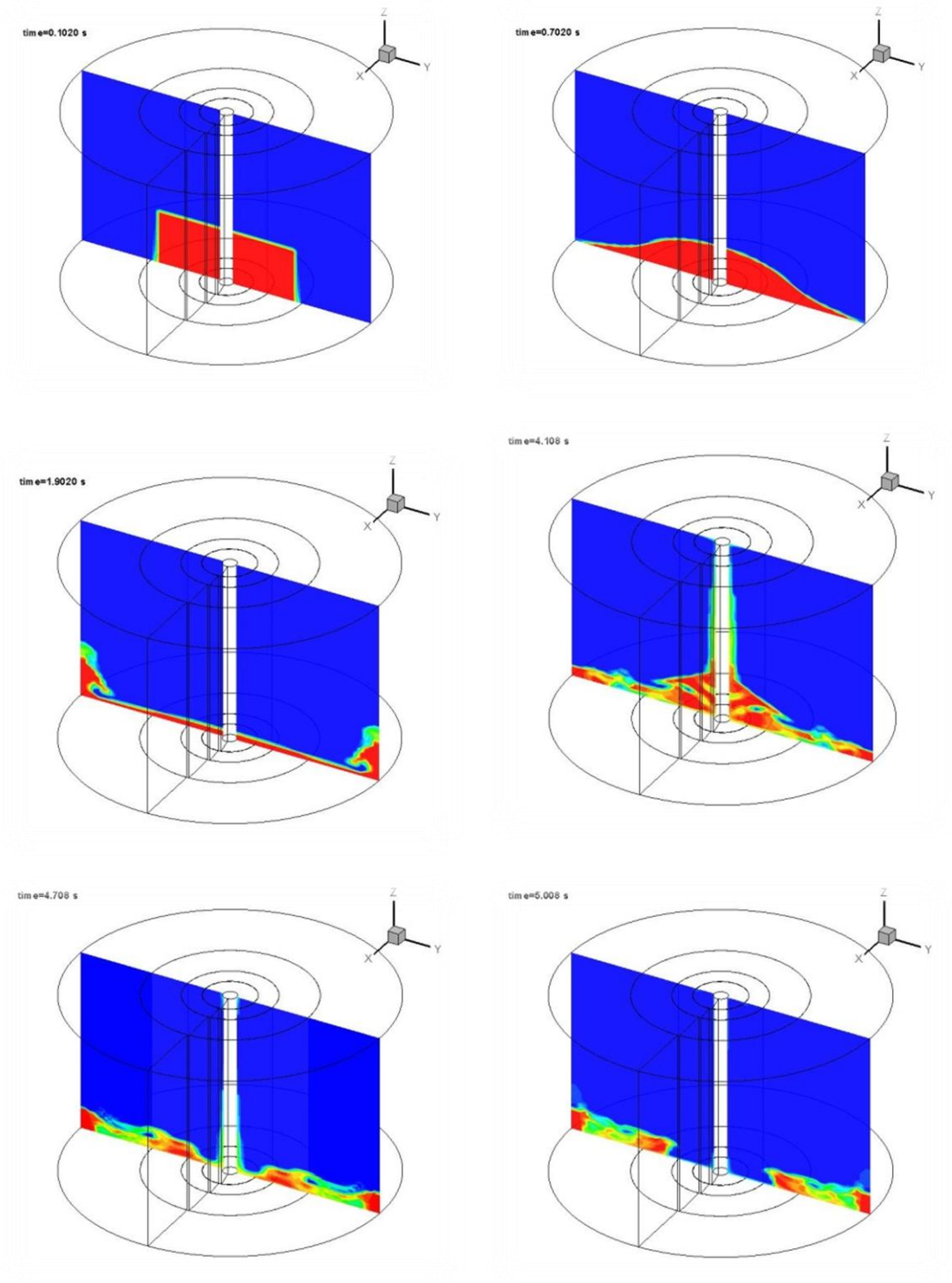

Fig. 2-16. Snapshots of free surface of circular dam at the section $rcos\theta = 0$.

The test cases include an idealized circular water dam breaking without azimuthal velocities and a three-dimensional water dam breaking in cylindrical tank with azimuthal velocities. In the first case, with a cylindrical symmetry water volume in the centre of the cylindrical tank, the symmetric shock-capturing capability of the proposed model is tested. In the other case, with a vertical dam set as a half concentric volume at the outer side of the cylindrical tank, fully three dimensional flow motions can be validated. The density and viscosity of the water phase and air phase are set to be 980 kg/m^3, 1.28 kg/m^3 and 1.01$\times 10^{-3} pa \cdot s$, 1.8$\times 10^{-5} pa \cdot s$ in these two cases.

2.8.1 Circular dam breaking

The circular dam breaking case is normally used to test capability of models for the symmetric free surface simulations by researchers (Lin et al, 2003; Erpicum, et al., 201; Zoppou and Roberts, 2000; Gottardi and Venutelli, 2004). In circular dam breaking case, the velocity component in the azimuthal direction should be zero everywhere in the whole computational time. And the water height gradient in the azimuthal direction should always be zero in any location.

The simulation condition used herein is similar with Liu et al. (2003), where the computation was carried out with a shallow water model. The circular volume of water is set as $16\Delta r \times 10\Delta z$ in a cylindrical tank with a scale of $32\Delta r \times 40\Delta z$. The two-dimensional contour of the vertical section $rcos\theta = 0$ shown in Fig 2-16 shows that the perfect symmetric flow behavior is simulated by this two-phase model and the process of the water dam hitting the outer wall and returning back is successfully reproduced.

Fig. 2-17 shows the snapshots of the free surface distribution in the cylindrical tank, and the perfect symmetric on the axis can also be seen in this figure. Comparing the results computed by the shallow water models, the free surface distribution in this figure is much more smoothed. The gradient of the free surface

distribution is almost zero everywhere and that agree with the results shown in Fig. 2-18, where the velocity component in azimuthal direction is zero everywhere and that is consistent with the characteristics of the circular dam breaking.

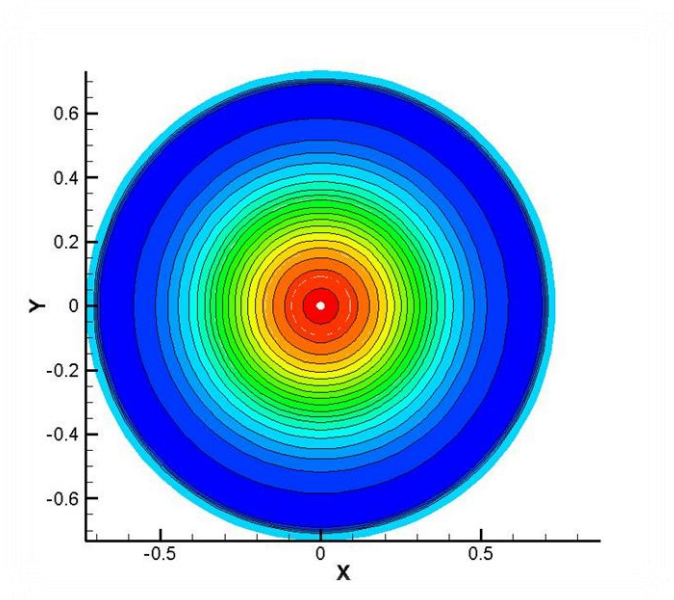

Fig. 2-17. Contour showing the water depth variation of the circular dam breaking at t=0.45 s ($16\Delta r \times 10\Delta z$).

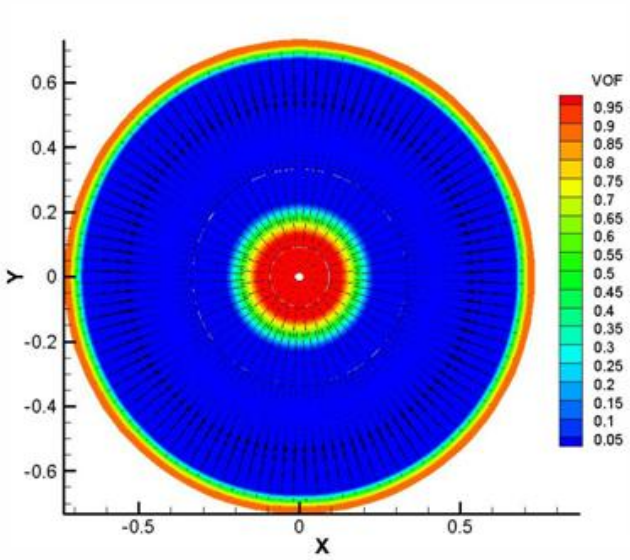

Fig. 2-18. Velocity components and VOF function in the slice $z = 4\Delta z$ at t=0.45 s.

From this case study, it is can be concluded that the present two-phase flow model is accurate to simulate two-phase incompressible flow movement. The VOF method developed for this cylindrical tank can track the free surface movement over the zonal embedded grids.

2.8.2 Three dimensional dam breaking

To demonstrate the proposed model is capable to simulate the fully three-dimensional flow motions, the three-dimensional water dam breaking in a cylindrical tank is tested herein over the zonal embedded grids that are uniform in r and z direction. The computational domain is shown in Fig. 2-19, where a semi-circular ($10\Delta r \times 10\Delta z$) volume of water is settled from $\pi/2$ to $3\pi/2$ at the out boundary side of the cylindrical tank ($32\Delta r \times 40\Delta z$). A small cylinder with a diameter $2\Delta r$ is installed in the center of the tank.

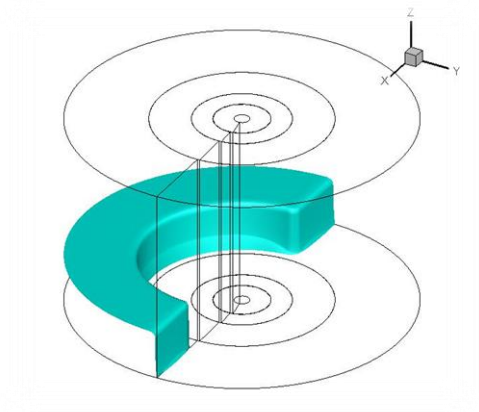

Fig. 2-19. Initial condition of three dimensional dam.

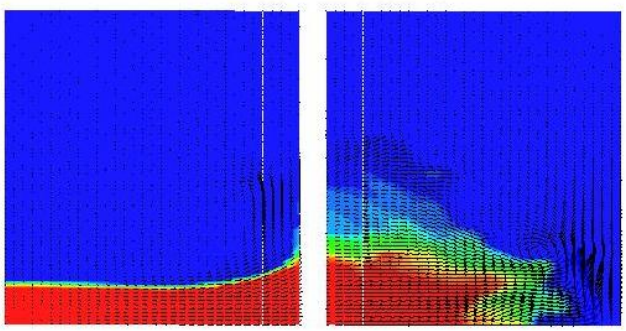

Fig. 2-20. free surface distribution and velocity filed at $t = 1.4\ s$ of section $rcos\theta = 0$.

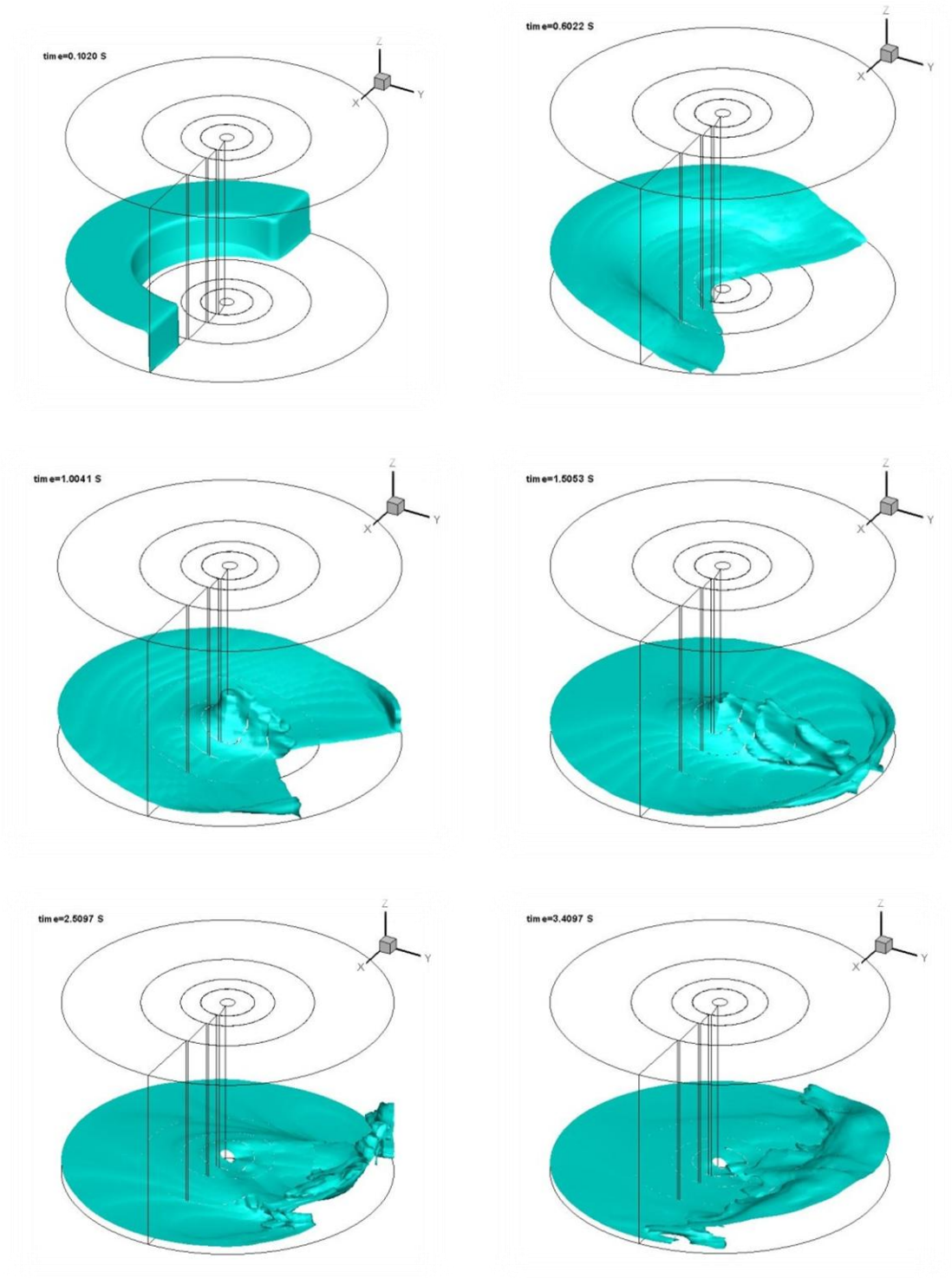

Fig. 2-21. Snapshots of free surface at different times

(three dimensional case).

The velocity field is shown in Fig. 2-20 and the snapshots of the free surface of the dam breaking in the tank at different time are shown in Fig. 2-21. It can be seen from the figures that the complex three-dimensional fluid motions can be simulated with this model, and the complex fluid surface near the small cylinder is captured very well.

2.9 conclusions

In the framework of the finite volume method, a proposed algorithm using the Projection method, and VOF method to track the free surface, was established by solving the Navier-Stokes equations over the zonal embedded grids. To preserve the accuracy, the NVD based high resolution scheme was used for the convection term of the Navier-Stokes equations. The linear equation was computed with a high performance AMG method. To track the free surface over the complicate embedded grids, the volume fraction convection equation was calculated with an algebraic CICSAM-VOF method, which is capable to avoid numerical diffusion.

Case studies of the proposed model were carried out to test the model. As no experiment studies can be found for the dam breaking in a cylindrical tank, the numerical experiments were used to check the numerical stability and the performance of this model. In the circular dam breaking, changes only happened in radial and vertical direction and the numerical experimental result showed the consistency of this phenomenon.

References:

Brackbill, J. Kothe, D. B. and Zamch, C., 1992. A continuum method for modeling surface tension. Journal of Computational Physics 100, 35-54.

Chorin, A. J., 1968. Numerical solution of the Navier-Stokes equations. Mathematics of Computation 22,745-762.

Darwish, M. S. and Moukalled, F., 1996. The normalized weighting factor method: a novel technique for accelerating the convergence of high-resolution convective schemes. Numerical Hear Transfer, Part B, 30217-237.

de Vahl Davis, G., 1979. A node on a mesh for use with polar coordinatess. Numerical Heat Transfer 2, 261-266.

Erpicum, S., Dewals, B. J., Archambeau, P. and Pirontton, M., 2010. Dam-break flow computation based on an efficient flux-vector splitting. Journal of Computational and Applied Mathematics 234, 2143-2151.

Ferziger, J. and Peric, M., 1996, Computational methods for fluid dynamics, Heidelberg: Springer.

Gaskell, P. H. and Lau, A. K. C., 1988. Curvature-compensated convective transport: SMART, a new boundedness-preserving transport algorithm. International Journal for Numerical Methods in Fluids 8, 617-641.

Gottardi, G. and Venutelli, M., 2004. Central scheme for two-dimensional dam-break flow simulation. Advances in Water Resources 27, 259-268.

Copala, V. G. and van Wachem, B. G. M., 2008. Volume of fluid methods for immiscible-fluid and free-surface flows. Chemical Engineering Journal 141, 204-221.

Harlow, F. and Welch, J. E., 1965. Numerical calculation of time-dependent viscous incompressible flow of fluid with free surface. Physics Fluid 8, 2182-2189.

He, T. L., Tao, W. Q., Qu, Z. G. and Chen, Z. Q., 2004. Steady natural convection in a vertical cylindrical envelop with adiabatic lateral wall. International Journal of Heat

and Mass Transfer 47, 3131-3144.

Heyns, J. A., Malan, A. G., Harms, T. M. and Oxtoby, O. F., 2013. Development of a compressive surface capturing formulation for modeling free-surface flow by using the volume of fluid approach. International Journal for Numerical Method in Fluids 71, 788-804.

Heyns, J. A., Harms, T. M. and Malan, A. G., Free surface modeling technology for compressible and violent flows, 41st AIAA Fluid Dynamics Conference and Exhibit, Honolulu, Hawaii, 27-30 June 2011.

Hirt, C. W. and Nichols, B. D., 1981. Volume of fluid (VOF) method for the dynamics of free boundaries. Journal of Computational Physics 39, 201-225.

Jasak, H., Weller, H. C. and Gosman, A. D., 1999. High resolution NVD differencing scheme for arbitrarily unstructured meshes. International Journal for Numerical Method in Fluids 31, 431-449.

Kravchenko, A. G., Moin, P. and Moser, R., 1996. Zonal embedded grids for numerical simulations of wall-bounded turbulent flows. Journal of Computational Physics 127, 421-423.

Lafaurie, B., Nardone, C., Scardoveli, R., Zaleski, S. and Zanetti, G., 1994. Modeling merging and fragmentation in multiphase flows with SURFER, Journal of Computational Physics 113, 134-147.

Leonard, B. P., 1991. The ULTIMATE conservation difference scheme applied to unsteady one-dimensional convection. Computer Methods in Applied Mathematics and Engineering 88, 17-74.

Lin, G.-F., Lai J.-S. and Guo W.-D., 2003. Finite-volume component-wise TVD schemes for 2D shallow water equations. Advances in Water Resources 26, 861-873.

Losasso, F., Fedkiw, R. and Osher, S., 2006. Spatially adaptive techniques for level set method and incompressible flow. Computer and Fluids 35, 995-1010.

Losasso, F., Gibou, F. and Fedkiw, R., 2004. Simulating water and smoke with an

octree data structure. ACM Transaction on Graphics 23, 457-462.

Notay, Y., AGMG software and documentation. see http://homepages.ulb.ac.be-/~ynotay/AGMG.

Osher, S. and Sethian, J. A., 1988. Fronts propagating with curvature-dependent speed: algorithms based on Hamilton-Jacobi formulation. Journal of Computational Physics 79, 12-49.

Popinet, S., 2003. Gerris: a tree based adaptive solver for the incompressible Euler equations in complex geometries. Journal of Computational Physics 190, 572-600.

Scardoveli, R. and Zaleski, S., 1999. Direct numerical simulation of free-surface and interfacial flow. Annual Review of Fluid Mechanics 31, 567-603.

Singh, R. and Shyy, W., 2007. Three-dimensional adaptive Cartesian grid method with conservative interface restructuring and reconstruction. Journal of Computational Physics 224, 150-167.

Suh, Y. K., and Yeo, C. H., 2006. Finite volume method with zonal-embedded grids for cylindrical coordinatess. International Journal for Numerical Methods in Fluids 52, 263-295.

Ubbink, O. and Issa, R., 1999. A method for capturing sharp fluid interfaces on arbitrary meshes. Journal of Computational Physics 153, 26-50.

Ubbink, O., 1997. Numerical prediction of two phase fluid systems with sharp interfaces. Ph.D. thesis, University of London.

Verzicco, R. and Orandi, P., 1996. A finite-difference scheme for the three dimensional incompressible flows in cylindrical coordinatess. Journal of Computational Physics 123, 402-414.

Xiao, F., 2005. A simple algebraic interface capturing scheme using hyperbolic tangent function. International Journal for Numerical Methods in Fluids 49, 1023-1040

Xue, S. C., Phan-Thien, N. and Tanner, R. I., 1999. Fully three-dimensional, time-dependent numerical simulations of Newtonian and viscoelastic swirling

flows in a confined cylinder: part I. Method and steady flows. Journal of non-Newtonian Fluid Mechanics 87, 337-367.

Yokoi, K., 2007. Efficient implementation of THINC scheme: a simple and practical smoothed VOF method. Journal of Computational Physics 226, 1985-2002.

Zalesak, S. T., 1979. Fully multi-dimensional flux corrected transport algorithm for fluid flow. Journal of Computational Physics 31, 335-362.

Zoppou, C. and Roberts, S., 2000. Numerical solution of the two-dimensional unsteady dam break. Applied Mathematical Modeling 24, 457-475.

Chapter 3

Numerical and experimental studies of tsunami-bridge interaction

3.1 Introduction

Tsunami usually caused by earthquakes, landslides or volcanic eruptions, is long water waves triggered by a sudden disturbance of the sea/ocean floor or surface. In deep water condition, tsunami can travel at celerities of 600-800 kilometers per hour. As the wave approaches shallow water region near the coast, wave celerity is reduced and the wave height significantly increases, sometimes exceeding 20 meters, reproduce high runups which can flood the coastal areas and even destroy a city.

Bridge failure has been a very series issue through the investigation of 2004 Indian Ocean tsunami and 2011 Tohoku tsunami. Maruyama et al. (2013) summarized the static data of field survey for bridge failure because of the tsunami in March 11, 2011 in Japan and reported that 252 bridges out of 1793 were damaged in this desaster. And bridge failure caused by tsunami was also reported in the Indian Ocean tsunami 2004 by Unjoh and Endoh (2006). It was reported that 81 spans were washed out or heavily damaged of 186 spans existed on the route from Banda Aceh to Meulaboh, Sumatra Island, Indonesia. In those accidents, superstructures of some bridges have been totally washed out several meters over the bridges.

Fig. 3-1. A tsunami wave crashes over a street in Miyako City in northeastern Japan on March 11 (source: National geographic).

It was reported by Unjoh et al. (2006) that bridges with connections between decks and piers or shear keys that are used to prevent horizontal movement were rarely damaged. Therefore, the drag force acting on the bridge by tsunami caused the failure. However, based on the surveying data from the great east Japan earthquake 2011, Kawashima (2012) found that bridges can be washed out by tsunami without breaking the stoppers from the pier, and then pointed out that decks of the bridge were lifted by tsunami lift force and then washed away by tsunami. The mechanism of the bridge damage by tsunami is shown in Fig. 3-2, which means both the drag and lift forces caused by tsunami play an important role in investigating bridge failures in tsunami.

In this chapter, physical experiments are carried out to investigate tsunami and bridge interaction. Both the drag and lift forces are measured in the cases that the bridge are fixed and movable. To determine the critical situation of bridge failures by analyzing the tsunami acting process using the camera videos taken from the physical experiments. Numerical experiments based on two-phase incompressible flow model are used to validate the conclusions based on the physical study, for much more detailed results can be computed by the numerical model based on incompressible

two-phase flow model.

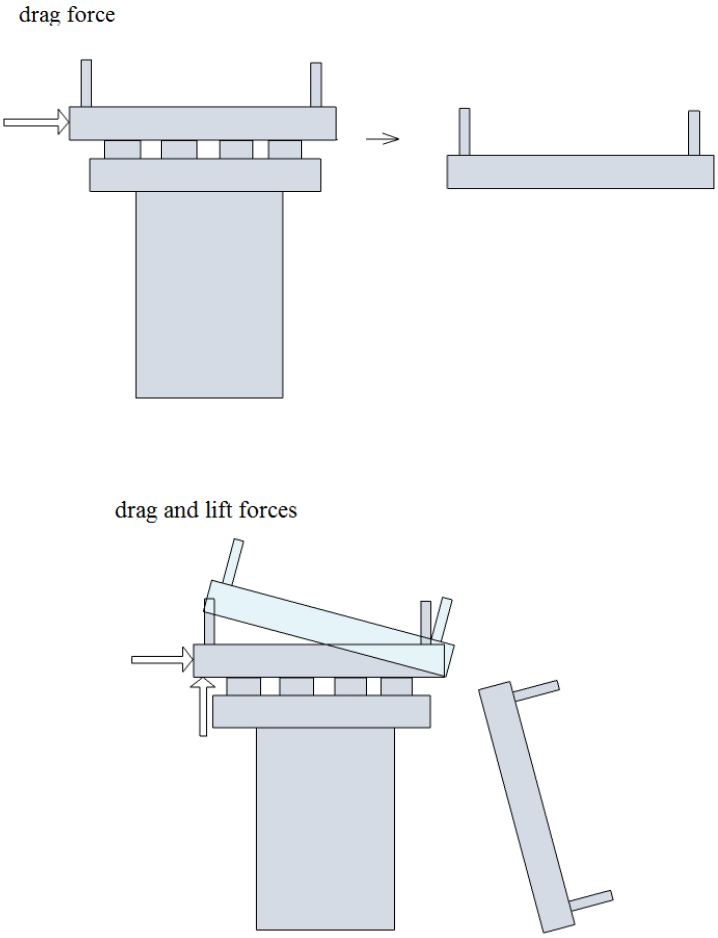

Fig. 3-2. Mechanism of the bridge damage due to tsunami

3.2 Experimental analysis

Another method to evaluate the tsunami acting force is to use the empirical formulas. Kosa et al. (2010) investigated the tsunami force acting on bridges after surveying the damage of bridges due to the tsunami in the Sumatra earthquake in 2004. In their study, the drag force acting on the bridge girder was explained by Eq. (3-1), as a function of the velocity of tsunami and the projected area of the bridge, which is as

similar as a hydro dynamic force, and the resistance of bridge, also named as fiction force, is mainly due to self weight was calculated by Eq. (3-2) or (3-3).

$$F_{xv} = \frac{1}{2} C_d \rho_w L_s H_s v^2$$
$$C_d = \begin{cases} 2.1 - 0.1B/D & \text{if } 1 < B/D < 8, \\ 1.3 & \text{if } 8 < B/D \end{cases} \tag{3-1}$$

$$S = \mu W, \tag{3-2}$$

$$S = \mu(W - F_b), \tag{3-3}$$

where C_d is the drag coefficient with its value determined in the reference (Japan Road Association, 2002), B and D are width and depth of the girder, ρ_w is the density of the water, v is the tsunami velocity, μ is the friction coefficient (0.6, based on the research by Rabbat et al. (1985)), W is the girder's self weigh (*kN*) and F_b is the buoyancy (*kN*) computed by Eq. (3-4).

$$F_b = \rho_w g V. \tag{3-4}$$

where V donates the volume of the bridge girder immerged under the water surface. In this study, the formula of the drag force is used to be a comparison result of the experimental study.

A series of hydraulic experiments is carried out based on Froude similarity with a length scale of 1/50 in the section wave tank of the Department of Civil Engineering, Nagoya University, Japan (12.5m×2.22m×1.0m) with a piston-type wavemaker of the maximum stroke of 1.5m installed in the wave tank. Tsunami is generated with the piston-type wavemaker in the wave tank. Pressure is measured to compute the tsunami action forces and the tsunami velocity is needed to determine the empirical tsunami action forces calculated by Eq. (3-1).

3.2.1 Experimental setup

Fig. 3-3 and Fig. 3-4 show the details of the setup of the experimental study, where the section tank is divided into three small channels and all these three 31 cm wide

channels are facing the same wavemaker. The same wave fields can be generated in the three channels by the wavemaker in the wave tank. A movable bridge model is settled in the first channel and the process of the tsunami acting on the bridge is recorded by a camera to find whether the bridge is moved or not and determine the critical situation in the tsunami acting history. In the second channel, a fixed bridge is installed to measure the wave force acting on the bridge and the tsunami profiles are measured in the last channel with four wave gauges.

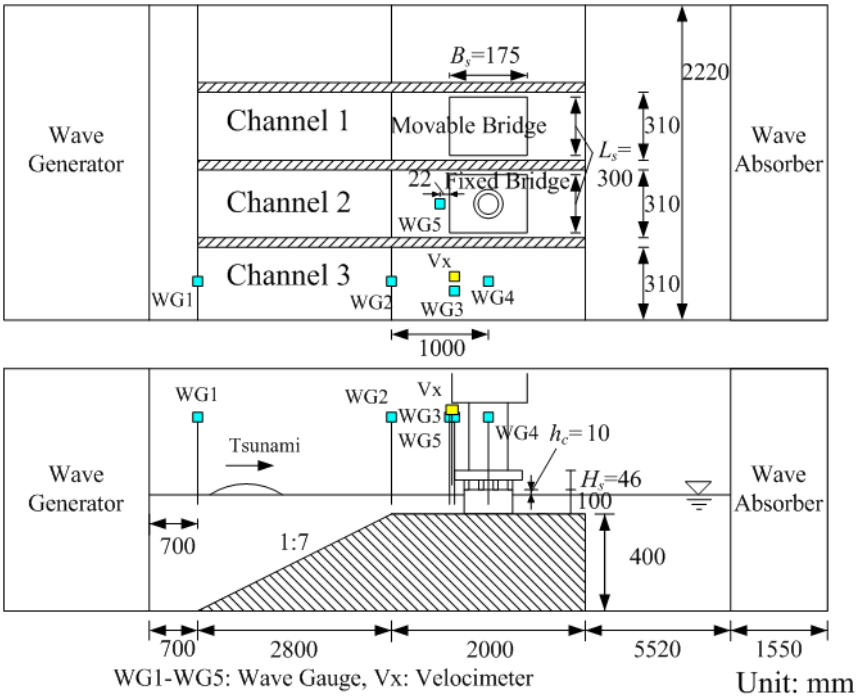

Fig. 3-3. Setup of experiment

Two bridge models, one is fixed and another is installed on the acrylic supporters, with a scale shown in Fig. 3-5, are fixed in the channels on a 40 cm high platform. In the sea side of the platform, there is a 1:7 slope to simulate the topography of the sea bed. The bridges are settled 1 cm above the water surface. Tsunami is generated by the long period movement of the wavemaker in the section wave tank where the water depth is 49 cm.

Tab. 3-1. Experimental cases

Case	*T* [s]	*S* [m]	*H* [mm]	Bridge motion
1-1	16	0.82	42.6	Not moved
1-2		0.82	42.5	Slightly moved
1-3		0.86	44.5	Slightly moved
1-4		0.86	44.4	Slightly moved
1-5		0.90	45.8	Slightly moved
1-6		0.90	45.6	Fell
2-1	20	1.06	40.3	Not moved
2-2		1.06	40.1	Not moved
2-3		1.10	41.7	Slightly moved
2-4		1.10	41.6	Slightly moved
2-5		1.14	42.9	Fell
2-6		1.14	43.2	Fell
3-1	24	1.16	35.1	Not moved
3-2		1.16	35.4	Not moved
3-3		1.20	37.2	Fell
3-4		1.20	37.2	Fell
3-5		1.24	38.6	Fell
3-6		1.24	38.5	Fell
4-1	28	1.26	34.8	Not moved
4-2		1.26	34.7	Not moved
4-3		1.30	36.5	Slightly moved
4-4		1.30	36.2	Slightly moved
4-5		1.34	38.2	Fell
4-6		1.34	38.4	Fell
5-1	32	1.38	36.2	Not moved
5-2		1.38	35.8	Not moved
5-3		1.42	36.8	Fell
5-4		1.42	37.2	Fell
5-5		1.46	38.0	Fell
5-6		1.46	37.7	Fell

As shown in Tab. 3-1, in the physical study, cases are categorized by the periods and strokes of the wavemaker movement, where T, S is period and stroke of the wavemaker movement which are the main parameters to set the wavemaker, H is the

measured wave height. The situations of the bridge are presented in the fifth column.

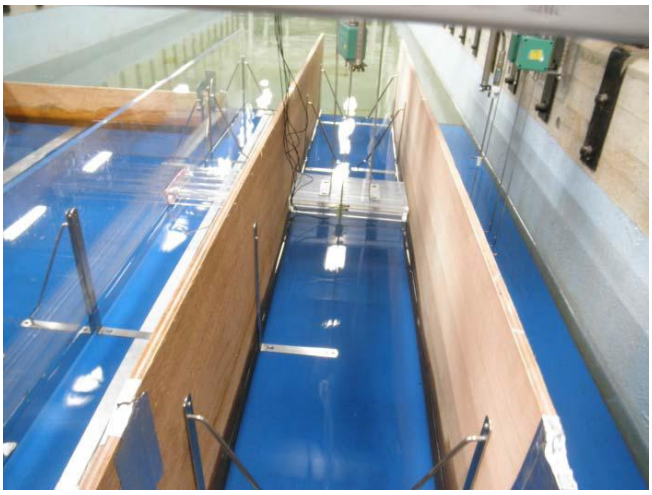

Fig. 3-4. Bridge models

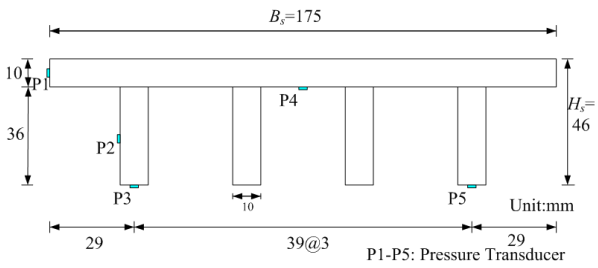

Fig. 3-5. Cross section of bridge model and locations where pressure transducers are installed

3.2.2 Experimental results and discussion

Fig. 3-6 shows the good agreement of the horizontal wave force computed by Eq. (3-1) and the one measured with the face transducer in the experiment. Since the velocity is measured in the third channel where there is no structure, where the tsunami flows off without any resistance, so that the horizontal force calculated from Eq. (3-1) cannot explain the fact very well after the value of the wave force achieving to the maximum. That means Eq. (3-1) is an accuracy method to evaluate the wave force although it cannot explain the whole acting process of the tsunami drag force. As it is

shown in this figure, the horizontal force acting on the bridge gradually increases after the tsunami impinges the bridge, and reaches its maximum in 5 s after the impingement.

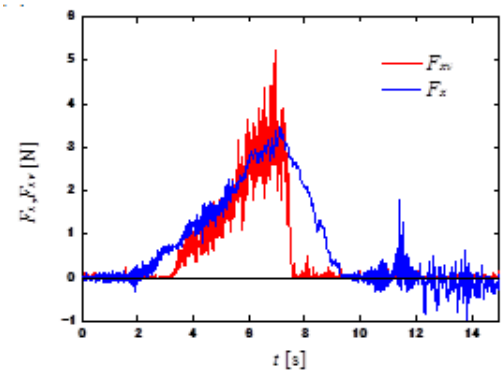

(a) Case 2-1 (*T=20 s*, *S=1.06 m*, not moved)

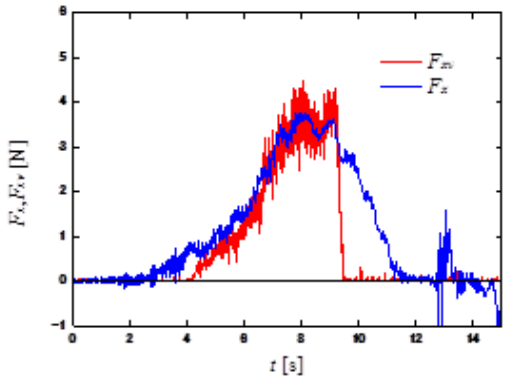

(b) Case 3-3 (*T=24 s*, *S=1.2 m*, fell)

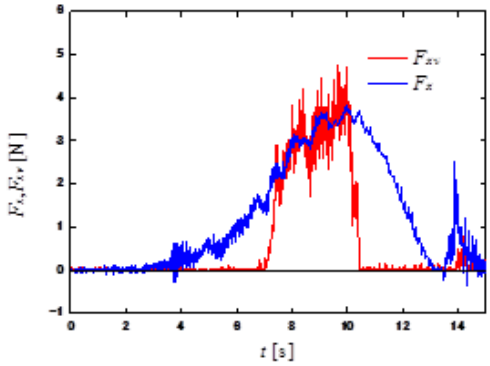

(c) Case 4-3 (*T=20 s*, *S=1.06 m*, slightly moved)

(d)

Fig. 3-6. Horizontal wave forces acting on bridge model

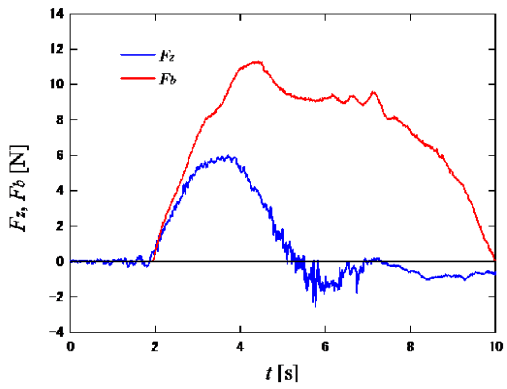

(a) Case 2-1 (*T=20 s, S=1.06 m*, not moved)

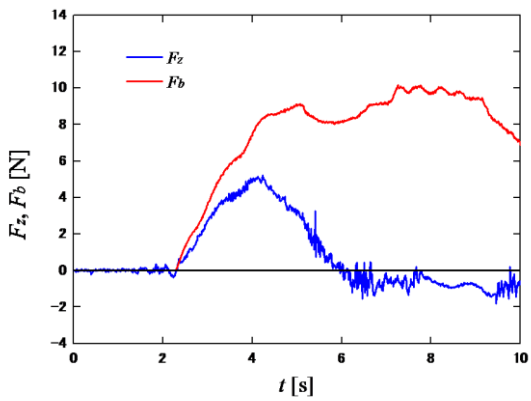

(b) Case 3-3 (*T=24 s, S=1.2 m*, fell)

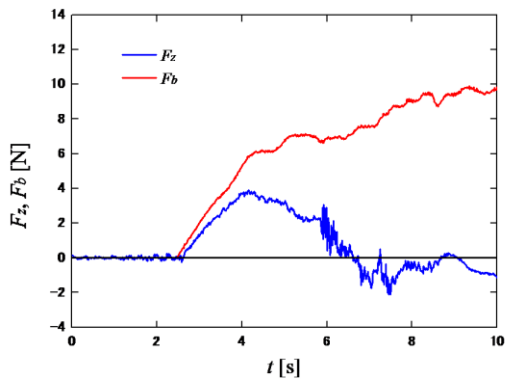

(c) Case 4-3 (*T=28 s, S=1.3 m*, slightly moved)

Fig. 3-7. Vertical wave forces acting on bridge model

From experimental data shown in Fig.3-6, it can be seen that the wave drag force

plays an important role in bridge failure. The maximum of the drag force in the case (3-3) where the bridge is washed out is much bigger than those in the cases (2-1) and (4-3). Although the maximum in case (4-3) where the bridge is slightly moved is only a little greater than that in case (2-1) where the bridge is not moved, the duration of the tsunami history is much longer. In a word, both the drag force and the duration of the tsunami affect the bridge facing to tsunami.

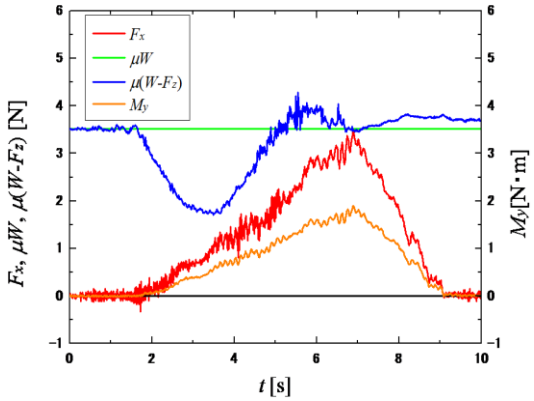

(a) Case 2-1 (*T=20 s, S=1.06 m*, not moved)

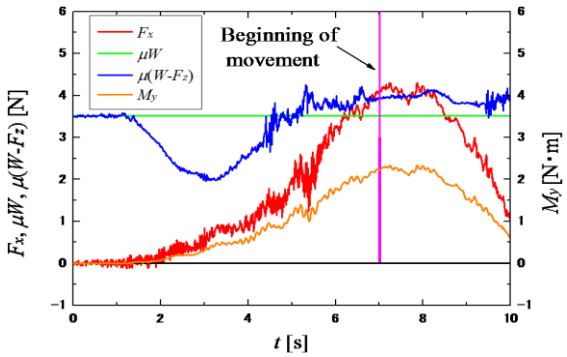

(b) Case 3-5 (*T=24 s, S=1.24 m*, fell)

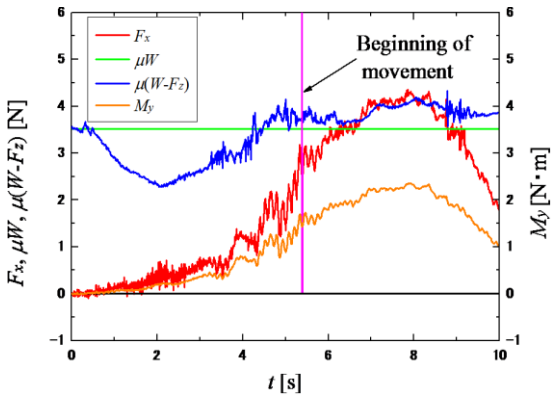

(c) Case 4-5 (*T=28 s, S=1.3 m*, fell)

Fig. 3-8. Wave forces and fiction force acting on bridge model

As discussed in section 3.1, not only the drag force but also the lift force is important to analyze the reason of bridge failures. Bridges may be lifted and washed out by tsunami. Fig. 3-7 represents the lift force measured from the experiment and the buoyancy force computed by Eq. 3-4. It is shown that the lift force is about more than 2 times bigger than the drag force in the case that bridge is not moved and the acting profile of the lift force is quite different with that of the drag force. The lift force is more quickly to achieve a high enough value than the drag force. In case (2-1) can be seen that the lift force achieves the maximum with about 2 second and the drag force with about 6 second and the lift force can be nearly 6 times bigger than the drag force at 4 second during the tsunami hitting. That can explain that the bridge is lifted firstly and then washed away by the tsunami.

The lift force also affects the horizontal force because the friction force depends on the vertical forces, and the friction force is the resistance to the horizontal movement by the action of the drag force. In Fig 3-8, the comparisons of friction value and drag force are presented. The critical situation is also given in this figure. It is can be seen that the friction force decreases as the tsunami start to affect the bridge. In cases 3-5 and 4-5 that the bridge is observed to be washed out, their friction forces measured in the experiment are smaller than the drag force when they start moving.

The bridge is expected to start moving when the drag force exceeds the friction force. In case 2-1, where no movement of the bridge is observed, Fig 3-8(a) indicates that the friction force is always bigger than the drag force. It is should be mentioned that since the forces are measured in the fixed bridge model at the second channel, the forces are not correct after the movement of the bridge model. To know the entire process of the tsunami action, numerical study is necessary to carry out.

3.3 Numerical analysis

The numerical work is achieved using a three-dimensional two-phase flow model with IB method to track the structure movement (Nakamura et al., 2011), which is based on the large-eddy simulation model for turbulence calculation and the volume of

fluid method for capturing the moving free surface.

Fig. 3-9 shows a schematic view of the computational domain from an experiment setup of Nakao et al. (2010). The tsunami is generated by the dam breaking of a volume of water. A movable bridge model with the dimensions of $80mm \times 200mm \times 20mm$ is fixed at a height of $65mm$ from the bottom of the tank. The bridge density is set as 1000, 1500, 2000 and 2500 kg/m^3 for the four cases respectively.

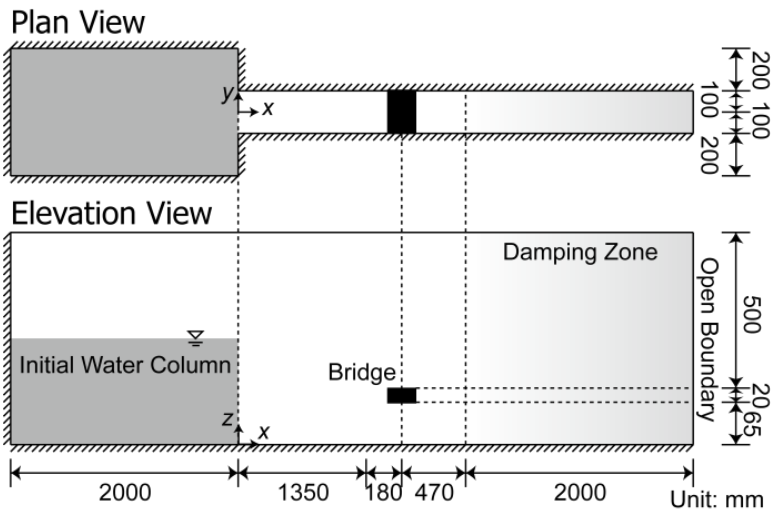

Fig. 3-9. Computational domain.

3.3.1 Numerical results and discussions

Fig. 3-13 shows the interaction process of tsunami and the bridge in the case that bridge density is 2000 kg/m^3. In this process, tsunami impinges the bridge around 1.4 s and the bridge is lightly moved at 2.6 s. The history of the forces of this process in that case can be seen in Fig. 3-10(c). The drag force F_x and the vertical force F_z gradually increases after tsunami start acting on the bridge and the bridge start moving when the drag force is bigger than the fiction force around 2.6 s. Fig. 3-10 shows the time histories of the forces acting on the bridge and the states of the bridge in the four cases. Fig. 3-12 (a) and (c) show the moment that the vertical force achieved the minimum. At that time, the bridge is totally under the tsunami wave surface and low pressure is achieved under the bridge because of vertex shedding. The

bridge starts to move when the drag force exceeds the fiction force and bridge failure happens as shown in Fig. 3-10 (a) and (b).

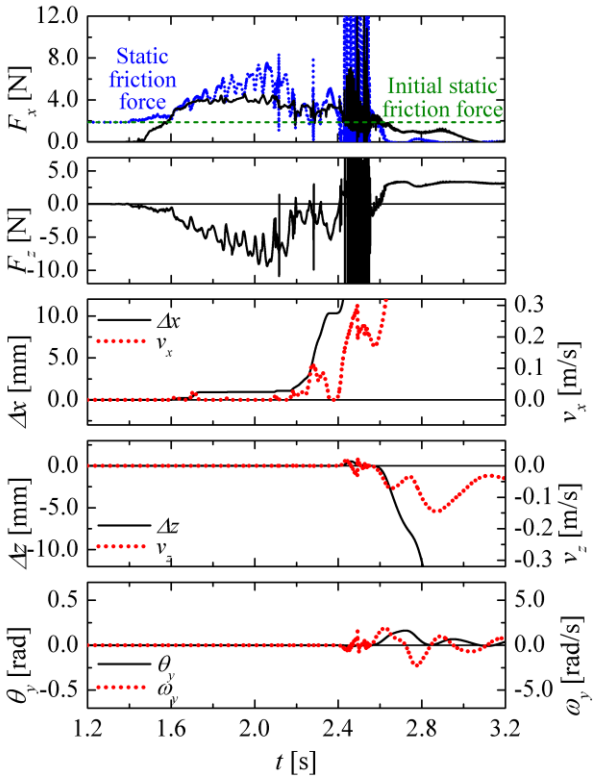

(a) $\rho_b = 1.0\times10^3$ kg/m^3

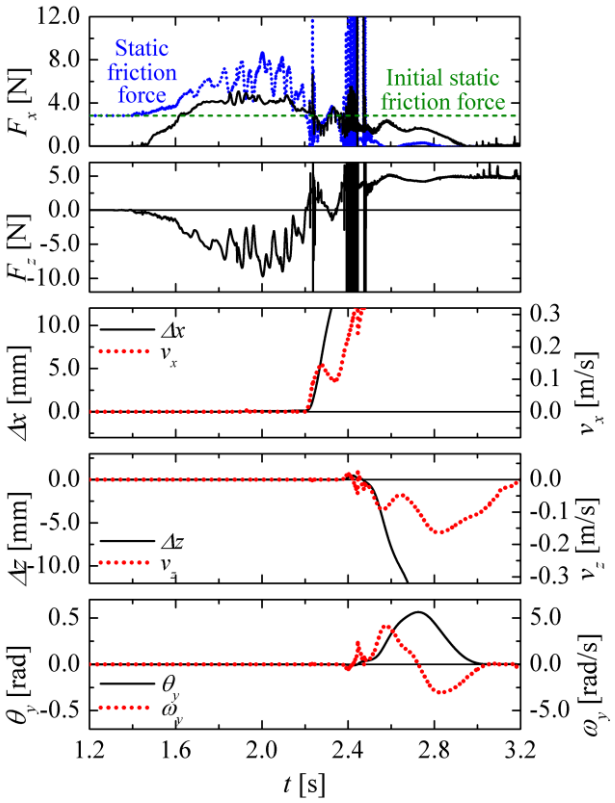

(b) $\rho_b = 1.5\times10^3$ kg/m^3

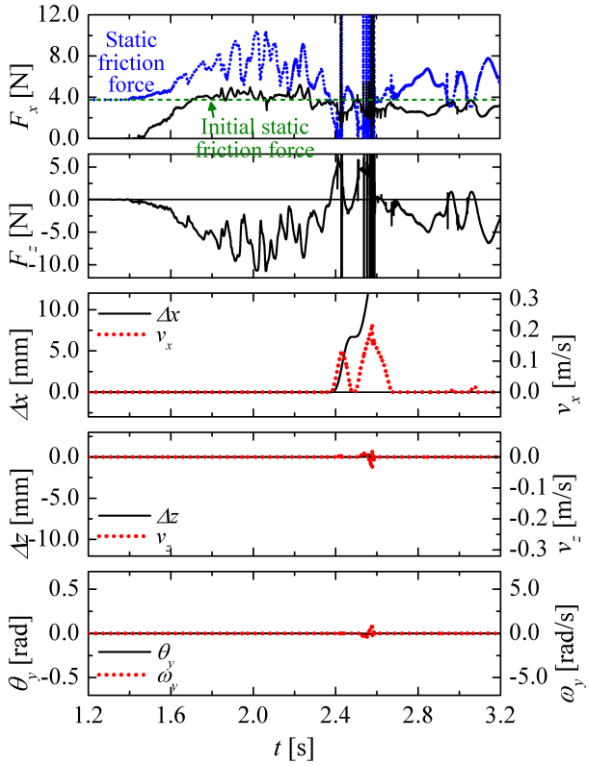

(c) $\rho_b = 2.0\times10^3$ kg/m^3

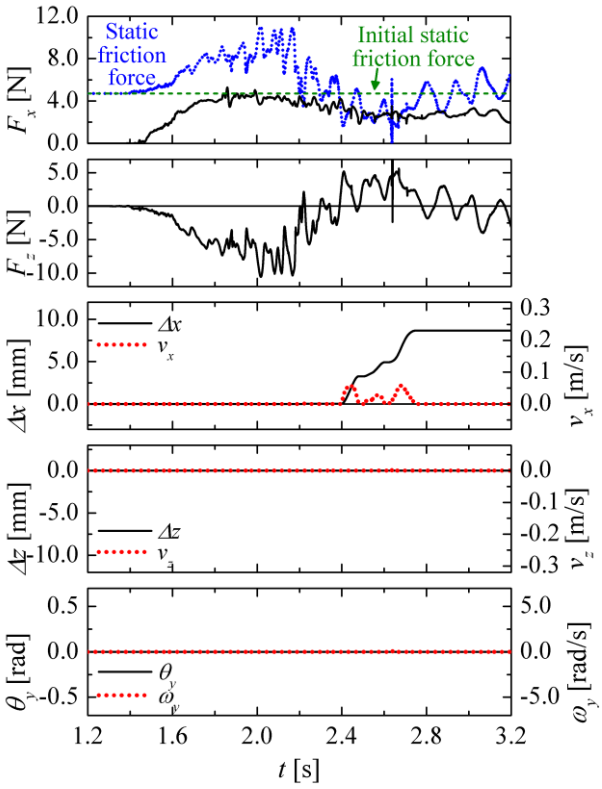

(d) $\rho_b = 2.0\times10^3$ kg/m^3

Fig. 3-10. Action forces of tsunami and responses of bridge.

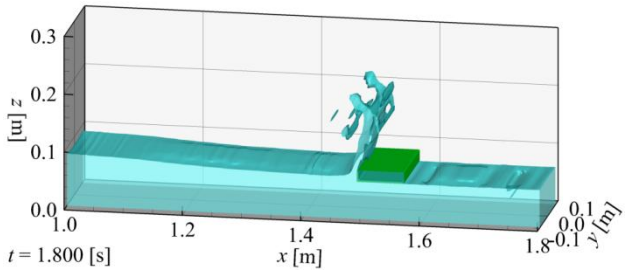

Fig. 3-11. Snap-shot of tsunami action on bridge.

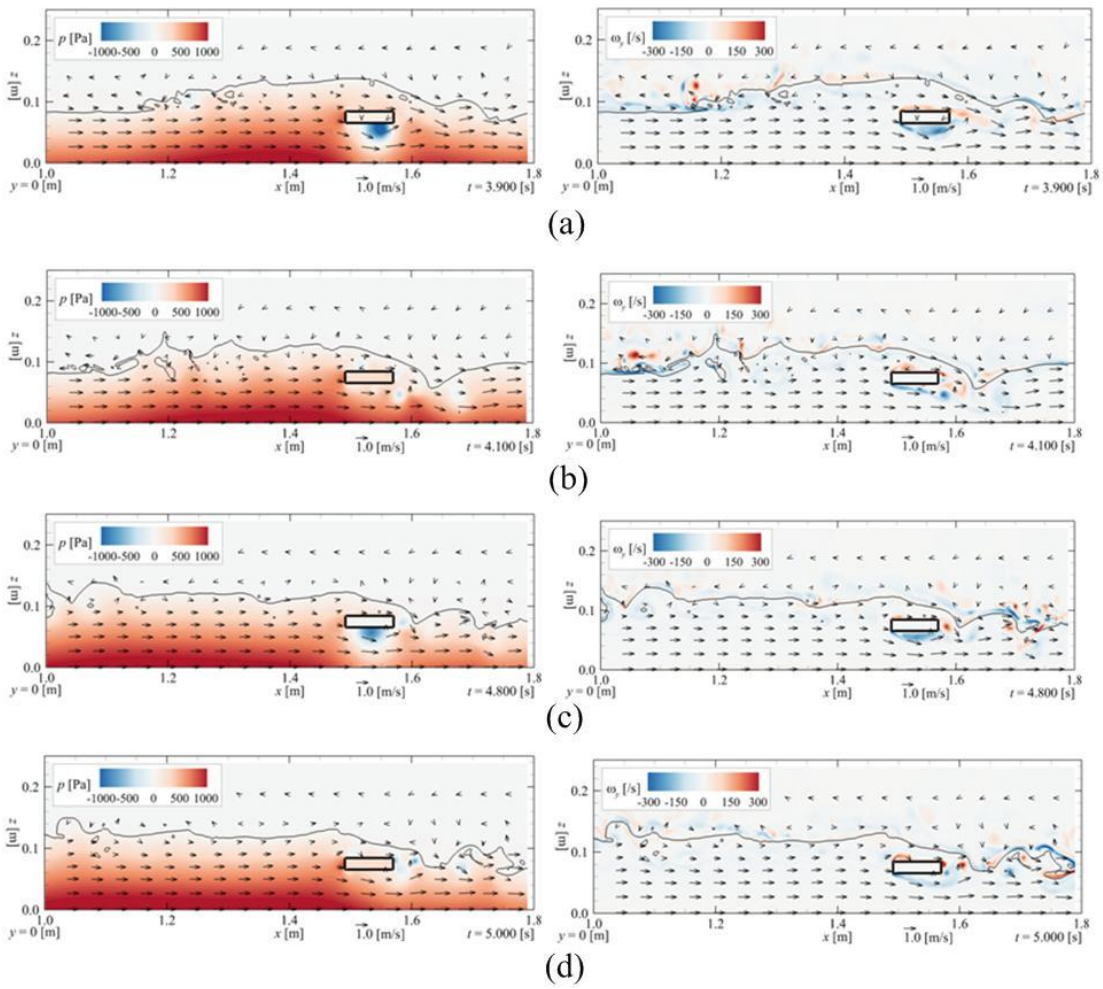

Fig. 3-12. Pressure and velocity distribution along y=0.0 m plane at time: (a) vertical forces achieved the minimum and (b) vertical forces achieved the maximum in case bridge density is 1000 kg/m^3, (c) vertical forces achieved the minimum and (d) vertical forces achieved the maximum in case bridge density is 1500 kg/m^3.

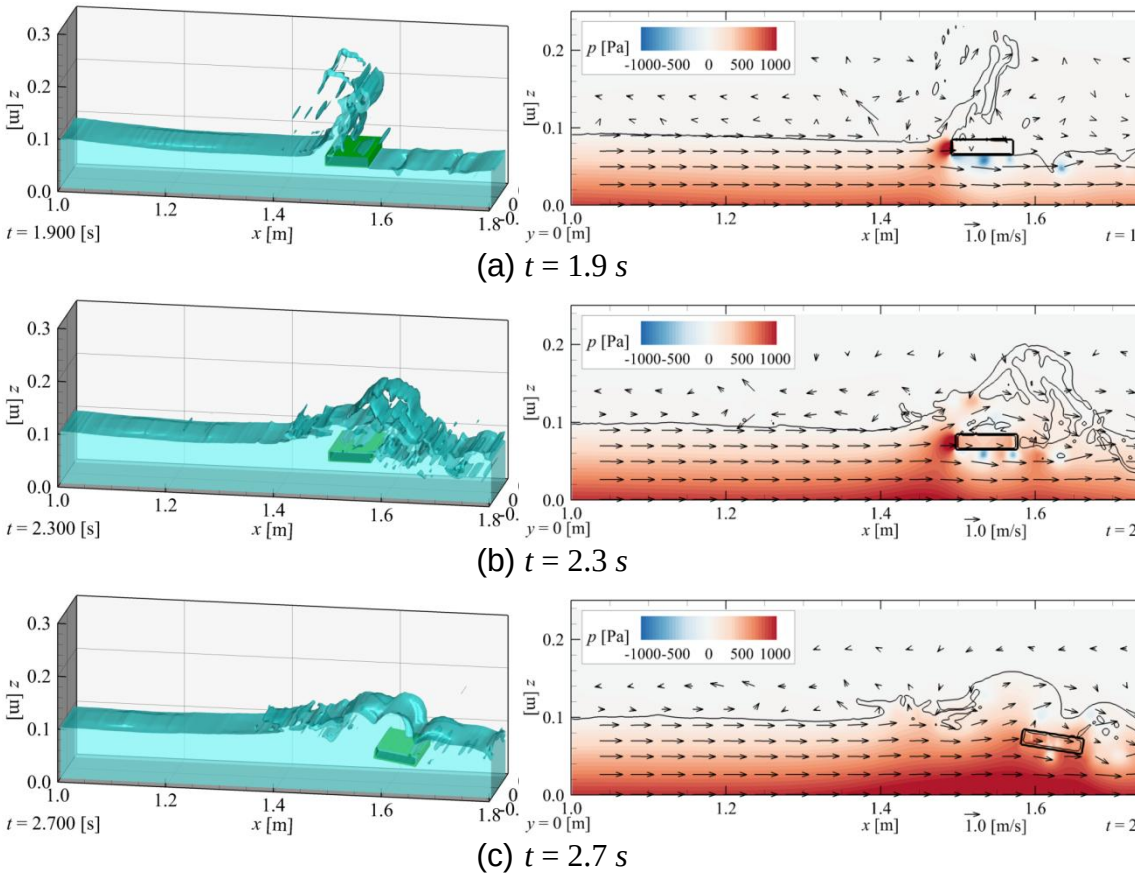

Fig. 3-13. Process of bridge that is washed out by tsunami

In Fig. 3-10 (c) and (d), since the bridge gravity is large enough to supply bigger friction forces to the bridge, the bridge is slightly moved in the case (c) and not moved in the case (d). Form the acting history of vertical and drag forces, two peaks can be seen. Kosa et al. (2010), using experimental data, found out that both horizontal and vertical forces reached a peak before the tsunami wave height became high. At the time the friction force decreases to the minimum, the bridge has been entirely immerged into the water. Since the velocity under the bridge is much bigger than the velocity above the bridge and the pressure under the bridge is much smaller after the bridge immerged into the tsunami wave, vertical forces start increasing until it achieve to the maximum, which is shown in Fig 3-12 (b) and (d). The vertical force will affect the friction force which is treated as the main factor of the stability of the bridge in this study.

3.4 Simulation of tsunami-bridge interaction with circular basin

The circular basin could be used to study tsunami-bridge interaction based on the two-phase incompressible flow model built in Chapter 2. In this section, a vertical cylinder is used to model the bridge pier and tsunami is generated by the dam breaking of a volume of water. Fig. 3-14 shows the computational domain where the vertical pier is set in the middle of the circular basin.

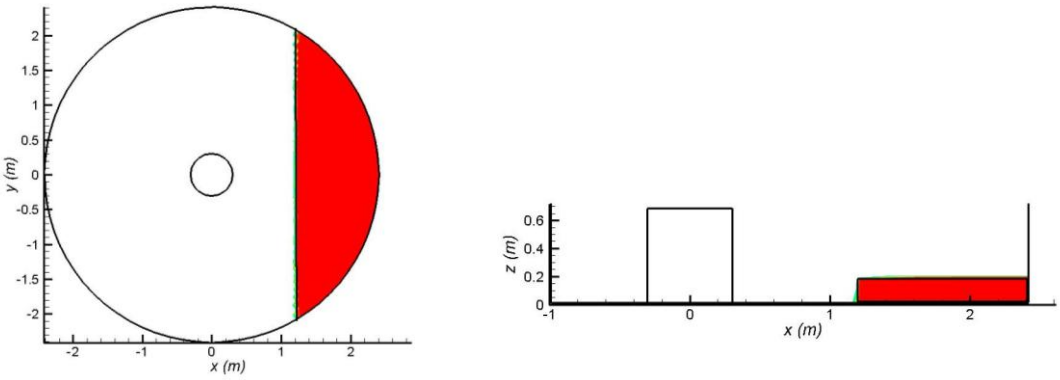

(a) Plan view (b) Elevation view

Fig. 3-14. Computational domain.

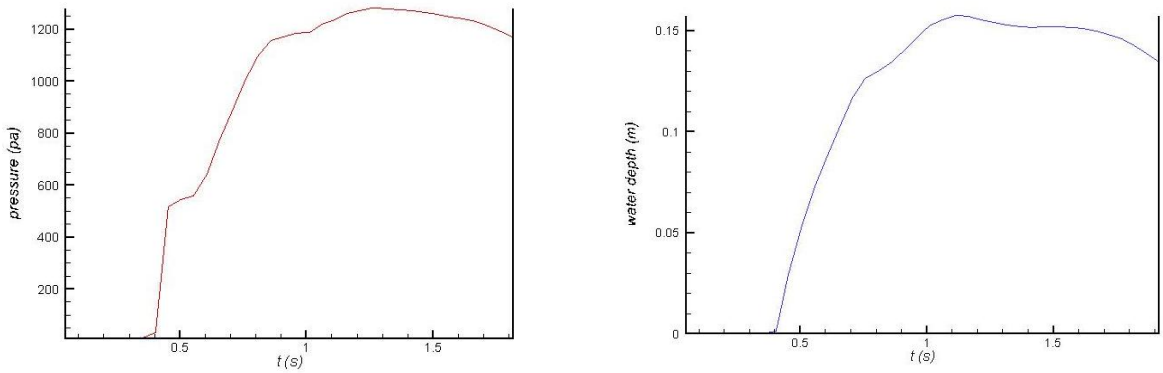

(a) (b)

Fig. 3-15. Pressure measure at 0.02 *m* depth and wave height at front of pier.

Fig. 3-15 shows the measured wave height and pore pressure at 0.02 *m* depth at the front of the pier. Those can explain that the present model can be used to model

tsunami-bridge interaction.

Tsunami can be simulated to hit the rectangular pier in different angles in the circular basin, so further researches will be carried out to study the interaction of tsunami and rectangular bridge pier by remodeling the present model with unstructured grids.

3.5 Conclusions

The investigation of the bridge-tsunami interaction is carried out based on a one-fluid formulation for incompressible three-dimensional multiphase flows, with the volume of fluid method to track the free surface and immersed boundary method to track the movement of the bridge and physical studies in the two-dimensional wave tank in Nagoya University.

The results showed that slowly-varying drag force loading on the bridge with long duration caused the failure, which coincided with the investigation of the 2004 Indian Ocean tsunami, where the main force that washed out the deck was the drag force and bridges with shear keys and connections between superstructure and substructure were rarely damaged in that disaster (Unjoh et al., 2006).

The horizontal drag force was affected by the tsunami and bridge section. The results showed that there was one peak of drag force in case of big vertical movement and there were two peaks of drag force in case of no or small vertical movement in the acting history of the horizontal component.

The vertical force played a very important role in the bridge failure problems. This suggested that the change of that force would cause a response of the friction force in the history of vertical component.

A simple simulation of the tsunami-bridge pier interaction in the circular basin was successfully achieved with tsunami generated by the dam breaking, which showed the proposed model can be used to simulate tsunami-bridge interactions. Future study will be carried out with a rectangular pier, in which case tsunami can hit the pier with different angles.

References:

Araki, S., Ishino, K. et al., Characteristics of tsunami fluid force acting on girder bridge. Preceeding of the 20th International Offshore and Polar Engineering Conference, Beijing, China, 2010.

Kawashima, K., Damage of bridges during 2011 great east Japan earthquake, Proceeding of the international symposium on engineering lessons learned from the 2011 great east Japan earthquake. March 1-4, 2012, Tokyo, Japan.

Kosa, K., Nii, S. et al., 2010. Analysis of damaged bridge by tsunami due to Sumatra earthquake. Journal of Structural Engineering, JSCE, 55A , 454-463 (in Japanese).

Lukkunaprasit, P., Lau, T. L. et al., Tsunami wave loading on a bridge deck with perforations. The 14th world conference on Earthquake Engineering, October 12-17, Beijing, China.

Nakamura, T., Yim, S. C. et al., 2011. Numerical simulation on local scouring around bottom-mounted movable short cylinder. Proceeding of Coastal structures 2011, ASCE, C4-087, 12pp.

Nakao, H., Izuno, K. et al., 2010. Study on relation of velocity and wave height to hydrodynamic force on bridges by tsunami. Journal of Structural engineering, ASME. 111, 564-575 (in Japanese).

Maruyama, K., Tanaka, Y. et al., Evaluation of tsunami force acted on bridges by great east Japan earthquake, 10th international conference on urban earthquake engineering. March 1-2, 2013, Tokyo Institute of Technology, Tokyo, Japan.

Rabbat, B. G., and Russel, H. G., 1985. Fraction coefficient of steel on concrete or grout, Journal of Structural Engineering, ASCE, 111, 505-515.

Shoji, G., Hiraki, Y. et al., 2011. Evaluation of tsunami fluid force action on bridge deck subjected to breaker bores. Procedia Engineering 14, 1079-1088.

Unjoh, S. and Endoh, K., 2006. Damage Investigation and the Preliminary Analyses of Bridge Damage Caused by the 2004 Indian Ocean Tsunami. Proceedings of the 38th UJNR Jiont Panel Meeting.

Wardhana K. and Hadipriono, F. C., 2003. Analysis of Recent Bridge Failures in the United States. Journal of performance of constructed facilities 17, 144-150.

Chapter 4

Development of circular wave basin model for oblique waves

4.1 Introduction

Wave tanks using wave generator to generate waves have been used for engineers to test wave properties about century. Laboratory and numerical wave generation techniques in two-dimensional wave tanks to reproduce the desired incident wave have reached maturity. As discussed in Chapter 1, the challenge is reproductions of oblique and multi-directional waves in three-dimensional wave basin, for the effective area is limited by wave refection and wave diffraction. Thus, Tanaka et al. (1994) proposed a new concept that waves were generated by the semi-circle wave source (Fig. 4-1) inside a circular wave basin without side walls. Based on this concept, both experimental and numerical studies had been carried out and results showed the practical improvement for the simulation of oblique waves for the effective area in the circular basin is significantly enlarged. Another advantage of this wave basin is that the effect of the incident angles of oblique waves to the effective area can be neglected.

In the present chapter, the circular wave basin model is developed based on the two-phase incompressible flow model proposed in Chapter 2 for deeper researches of

the circular wave basin, since only the inviscid and irrotational flow model is considered in the previous studies. To generate numerical waves in the circular wave basin, a transparent wave source method is applied within a semi-circle wave source zone. The semi-circle wave source zone is settled for the given waves according to the wave incident angles (Fig. 4-2) to make sure that the effect of the wave diffraction is as small as possible. Outgoing waves are dissipated in a dumping zone at the outer edge of the computational domain. To adopt this model, the continuous equation in the wave source zone is rewritten with a mass source term and momentum equations in dumping zone with a source term.

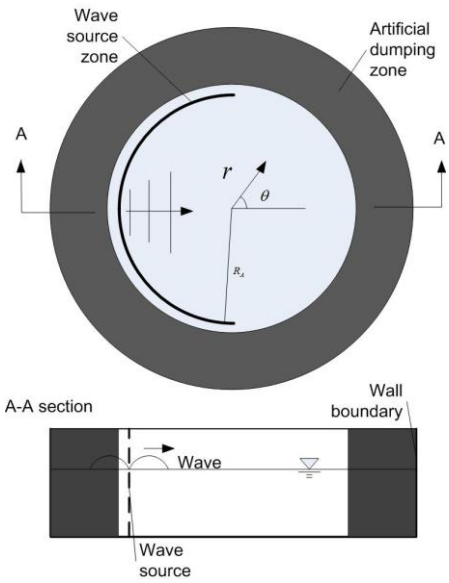

Fig. 4-1. Schematic sketch of circular basin

(first proposed by Tanaka et al. (1994)).

4.2 Wave source method

The transparent wave generation methods satisfy the need that they will not disturb the wave field for the outgoing waves will not be re-reflected by the wave generator. It has been used in different ways by Kawasaki (1999), and Lin and Liu (1999) in two-dimensional numerical wave models. With the wave source method, the original

continuity equation (Eq. (2-11)) and the volume fraction convection equation (Eq. (2-5)) in cylindrical coordinates could be modified as:

$$\frac{1}{r}\frac{\partial ru}{\partial r}+\frac{1}{r}\frac{\partial v}{\partial \theta}+\frac{\partial w}{\partial z}=Q(r_s,\theta_s,z,t)\,. \tag{4-1}$$

$$\frac{\partial F}{\partial t}+\frac{1}{r}\frac{\partial ruF}{\partial r}+\frac{1}{r}\frac{\partial vF}{\partial \theta}+\frac{\partial wF}{\partial z}=Q(r_s,\theta_s,z,t)F \tag{4-2}$$

where $Q(r_s,\theta_s,z,t)$ is the mass source term that is only non zero in the wave source zone; θ_i is the wave incident angle. The wave source zone (Fig. 4-2) used here located at $r=R_A$ is a volume below the instantaneous free surface with one grid width in a semi-circle.

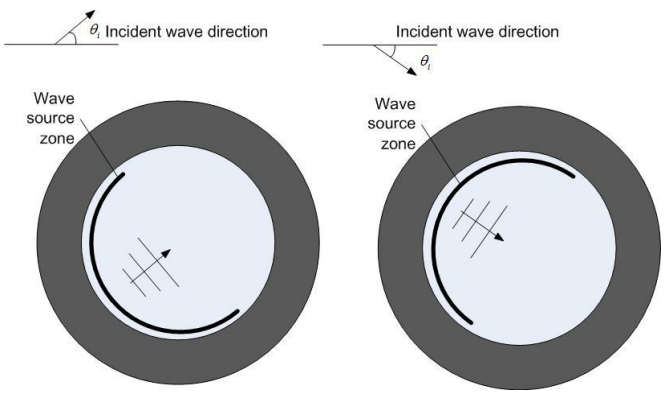

Fig 4-2. Setup of wave source zone $\theta_i-\frac{\pi}{2}\le\theta_s\le\theta_i+\frac{\pi}{2}$

(θ_i is the incident wave direction)

According to the wave theories, the wave source term can be derivated from the wave potential $\phi(r,\theta,z,t)$. Brorsen and Larsen (1987) gave the formula for the calculation of the mass source term, as:

$$\begin{aligned}Q(r_s,\theta_s,z,t)&=2\int_{-h}^{\eta}\int_{\theta_i-\pi/2}^{\theta_i+\pi/2}u(R_A,\theta,z,t)dzd\theta/V_s\\&=2\int_{-h}^{\eta}\int_{\theta_i-\pi/2}^{\theta_i+\pi/2}\frac{\partial\phi(R_A,\theta,z,t)}{\partial r}dzd\theta/V_s\end{aligned}, \tag{4-3}$$

where $V_s=\int_{-h}^{\eta}\int_{\theta_i-\pi/2}^{\theta_i+\pi/2}dzd\theta$, is the total volume of the wave source zone, and the coefficient 2 means waves are transported in both directions from the internal wave

source.

Lin and Liu (2004) dissipated the outgoing wave within a numerical damping zone using a source term added to the momentum equations, and this method is applied to the present circular wave basin to dissipate outgoing waves. The modified momentum equations in cylindrical coordinates are written as:

$$\frac{\partial u}{\partial t}+u\frac{\partial u}{\partial r}+\frac{v}{r}\frac{\partial u}{\partial \theta}+w\frac{\partial u}{\partial z}-\frac{v^2}{r}=-\frac{1}{\rho}\frac{\partial p}{\partial r}+ \frac{\partial}{r\partial r}(\nu\frac{\partial ru}{\partial r})+\frac{\partial}{r^2\partial\theta}(\nu\frac{\partial u}{\partial\theta})+\frac{\partial}{\partial z}(\nu\frac{\partial u}{\partial z})-\frac{\nu u}{r^2}-\frac{2\nu}{r^2}\frac{\partial v}{\partial\theta}+\frac{1}{\rho}F_{br}-f(r)u, \tag{4-4}$$

$$\frac{\partial v}{\partial t}+u\frac{\partial v}{\partial r}+\frac{v}{r}\frac{\partial v}{\partial \theta}+w\frac{\partial v}{\partial z}-\frac{uv}{r}=-\frac{1}{r\rho}\frac{\partial p}{\partial\theta}+ \frac{\partial}{r\partial r}(\nu\frac{\partial rv}{\partial r})+\frac{\partial}{r^2\partial\theta}(\nu\frac{\partial v}{\partial\theta})+\frac{\partial}{\partial z}(\nu\frac{\partial v}{\partial z})-\frac{\nu v}{r^2}-\frac{2\nu}{r^2}\frac{\partial u}{\partial\theta}+\frac{1}{\rho}F_{b\theta}-f(r)v, \tag{4-5}$$

$$\frac{\partial w}{\partial t}+u\frac{\partial w}{\partial r}+\frac{v}{r}\frac{\partial w}{\partial \theta}+w\frac{\partial w}{\partial z}=-\frac{1}{\rho}\frac{\partial p}{\partial z}-g+ \frac{\partial}{r\partial r}(\nu\frac{\partial rw}{\partial r})+\frac{\partial}{r^2\partial\theta}(\nu\frac{\partial w}{\partial\theta})+\frac{\partial}{\partial z}(\nu\frac{\partial w}{\partial z})+\frac{1}{\rho}F_{bz}-f(r)w, \tag{4-6}$$

where $f(r)$ is the fraction factor proposed by Lin and Liu (2004) in their two-dimensional wave model built in Cartesian coordinates. To implement this method to the circular wave basin, the original equation is reformulated into the form:

$$f(r)=\alpha\frac{\exp[(\frac{r-r_s}{r_e-r_s})^n]-1}{\exp(1)-1} \qquad r_s<r<r_e, \tag{4-7}$$

where r_s and r_e are the coordinates of the start and end edge of the dumping zone, and α and n the empirical coefficients chosen here as $\alpha = 200$ and $n = 4$.

For the boundary conditions, wall boundary is used in the seabed and the side boundary. In the top boundary of this wave basin over flow boundary is used, where the pressure is set as a constant value.

4. 3 Numerical experiments

In this section, the three-dimensional wave basin is tested for the real wave propagation problems. The computational domain is shown in Fig. 4-1 and the semi-circle wave source zone is set inside the computational zone and the dumping zone with a length of $80 \times \Delta r$ at the outgoing boundary. To demonstrate the capability of the developed numerical circular wave basin, results of the generation of oblique waves, including directional transition waves, two cross transition waves, are presented in this section.

Table. 4-1. Setup of zonal embedded grids

Blocks	M	6
I_M	1	4
	2-5	$2^{M-2} \times 4$
	6	120
J_M	1-6	$2^{M-1} \times 15$
K_M	1-6	80

The zonal embedded grid discussed in Chapter 2 is rearranged in this section to model the circular wave basin. Table 4-1 shows the setup of the mesh. In this model, the computational domain is divided into M blocks with the zonal embedded girds method, I_M, the number of radial grids, J_M, the number of azimuthal grids and K_M, the number of vertical grids in each block, are given by $I_M = I_0$, for $M = 1$, $I_M = 2^{M-2} I_0$ for $M \geq 2$, $J_M = 2^{M-1} J_0$ and $K_M = K_0$, where I_0, J_0 and K_0 are the number of grids in the first zone. Since coarser grids can be used in the dumping zone to save computation time, the grid number in radial direction of the last blocks where the dumping zone located is adjusted. The grids size is uniform in radial direction in the entire computational domain and in azimuthal direction in every block. In the

vertical direction, to track the free surface accuracy, non-uniform grids are applied to implement finer grids in the free surface region.

Table 4-2. Computational conditions

Cell size	Δr	0.03 m
	Δz	Minimum 0.005 m
Time step	Δt	Maximum 0.005 s (adjustable)
Wave period	T	1 s
Wave height	H	0.04 m
Water depth	h	0.6 m
Wave source location	R_A	3.0 m
Incident angle	θ_i	$\pi,\ 4\pi/3$

Substituting the potential of Airy wave into Eq. (4-3), the mass conservation form of the discretized mass source can be expressed as:

$$Q(r_s,\theta_s,z,t) = 2\frac{\int_{-h}^{\eta} u_r(r_s,\theta_s,z,t)dz}{\sum_{1}^{Kmax} u_r(r_s,\theta_s,z,t)\Delta z} u_r(r_s,\theta_s,z,t)/\Delta r\,. \tag{4-8}$$

$$u_r(r_s,\theta_s,z,t) = k\cos(\theta-\theta_i)\frac{gH}{\omega}\frac{\cosh k(h+z)}{\cosh kh}\cos(R_A\cos(\theta-\theta_i)-\omega t-p(\theta_s,t)) \tag{4-9}$$

where $Kmax$ is the index of the top node of the wave source zone in the vertical direction, k the wave number, η the wave elevation, H the wave height, ω wave frequency, g the gravitational acceleration, h water depth and $P(\theta_s,t)$ wave phase shift factor to maintain the numerical stability by making the mass source term start from zero. $Kmax$ is determined by the instantaneous free surface, and the index of the node that is chosen to be two cell height under the free surface in this model. The radius of wave source zone, R_A was chosen about 2 times of the wave length in this

model.

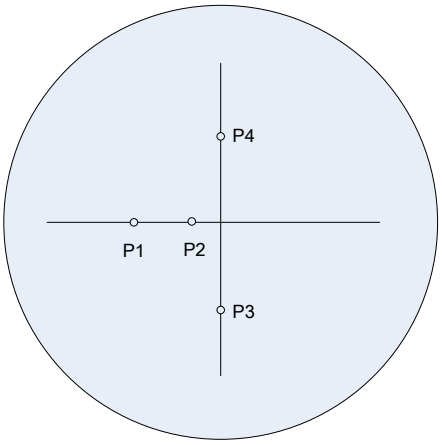

Fig. 4-3. Arrangement of wave gauges

(probe 1 ($r = 2\ m, \theta = \pi$), probe 2($r = 0.5\ m, \theta = \pi$),

probe 3 ($r = 2\ m, \theta = 3\pi/2$), probe4 ($r = 2\ m, \theta = \pi/2$))

4.3.1 Oblique waves simulation

A parametric cases are now performed for varieties of angles of wave generation. The incident angles chosen are $\theta_i = \pi$ and $\theta_i = 4\pi/3$, the wave period is 1 s and wave height is 0.04 m. William and Crull (2000) studied oblqiue waves with rectangular wave basin and found that the effective area of the wave basin was roughly triangular in shape. In the rectangluar wave basin, the triangular effective area affected by both the wave angle and width of the wave basin is bounded by reflected wave off the wall and the diffracted wave pattern. However, in the present model, the only factor affeted the effective area is the wave diffraction and it is decreased by the use of semi-circle wave generator, which is always normal to the wave propagation direction by setting the wave source zone. It can be seen from Figs. 4-4 and 4-5 that in a wide area of the wave basin the wave height distribution normalized with the incident wave height in the area $r \leq R_A$ is above 0.9 and the efective area for the the two cases is nearly same. Tanaka et al. (1994) based on their potential theory model,

figured out that the effective area was affected by R_A, the radius of the wave source zone. As the wave source is the not factor afecting the performance of the circular wave basin, studies will be carried out to test the circular wave basin with different R_A.

In this study, the affective zone is difined by that the value of the normalized wave height should be bigger than 0.9 and the radio of the effective zone to R_A for the two cases is about 0.75. Fig. 4-5 shows the wave height distribution along $x/L = -1$ and $x/L = -2$ of the cases $\theta_i = \pi$ and $\theta_i = 4\pi/3$, where the wave distribution is around 0.95. The Oblique wave generation with this model shows the perfect performace in mantaining the wave energe in the wide area. In other words, the effective area of this wave basin is enlarged and the effect of incident angle of waves to the effective area can be neglected in this circular wave basin.

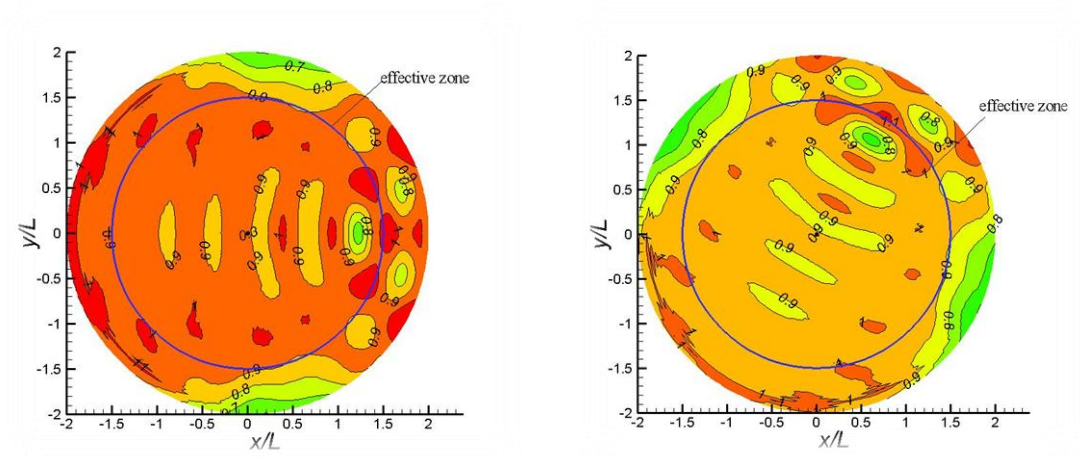

(a) (b)

Fig. 4-4. Wave height distributions of oblique wave $\theta_i = \pi$ and $\theta_i = 4\pi/3$.

In Fig. 4-6, 4-7 and 4-8, ressults of the reproduction of oblique waves have been represented. Figs. 4-6 and 4-7 show the time series of wave elevation colected at a set of wave guages. It is observed that the wave trains reach a stable state after two period movement and the profiles maintain uniform shapes after that. Typical nolinear

features, such as higher and narrower crests and smaller and flatter troughs are also obeserved. Fig. 4-8 exhibits the instantaneous wave surface elevation distincted by the differences of colors. Both the wave trains preserve the energy in most part of domain and the wave difraction happens at the two coners of wave source zone.

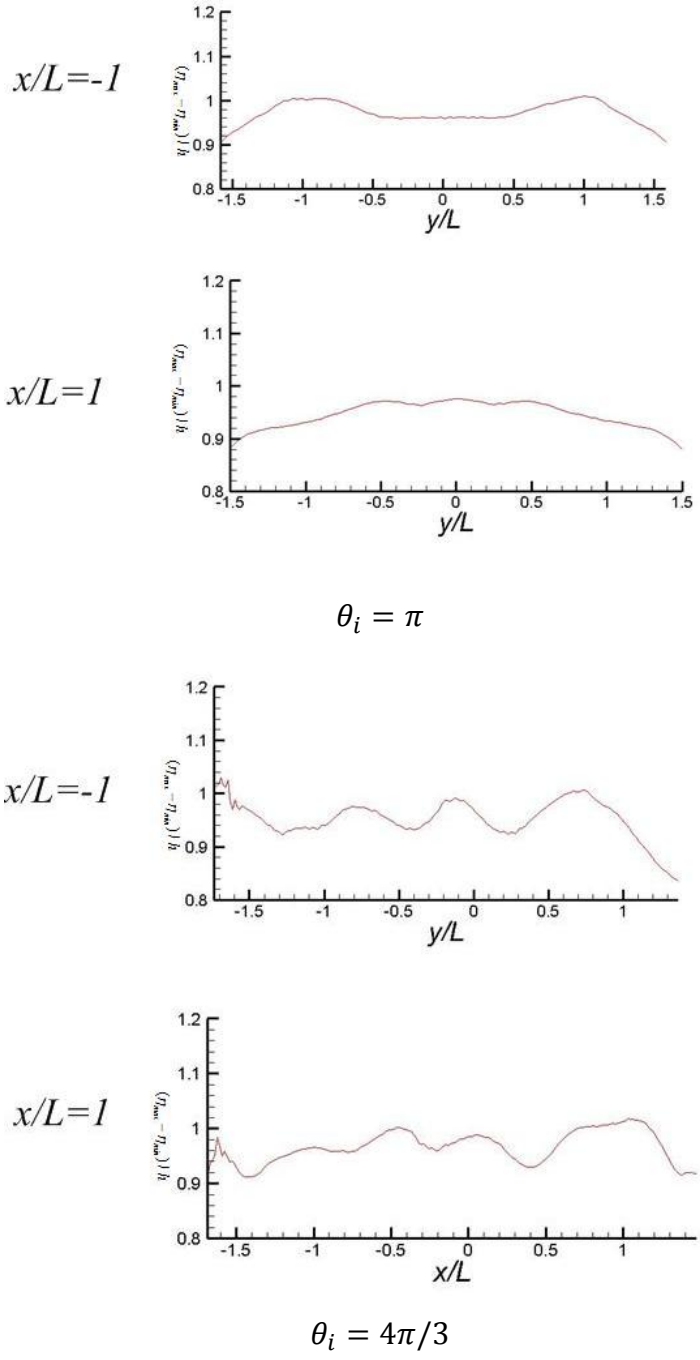

Fig. 4-5. Wave height distributions of oblique wave along $x/L = -1,\ x/L = 1$.

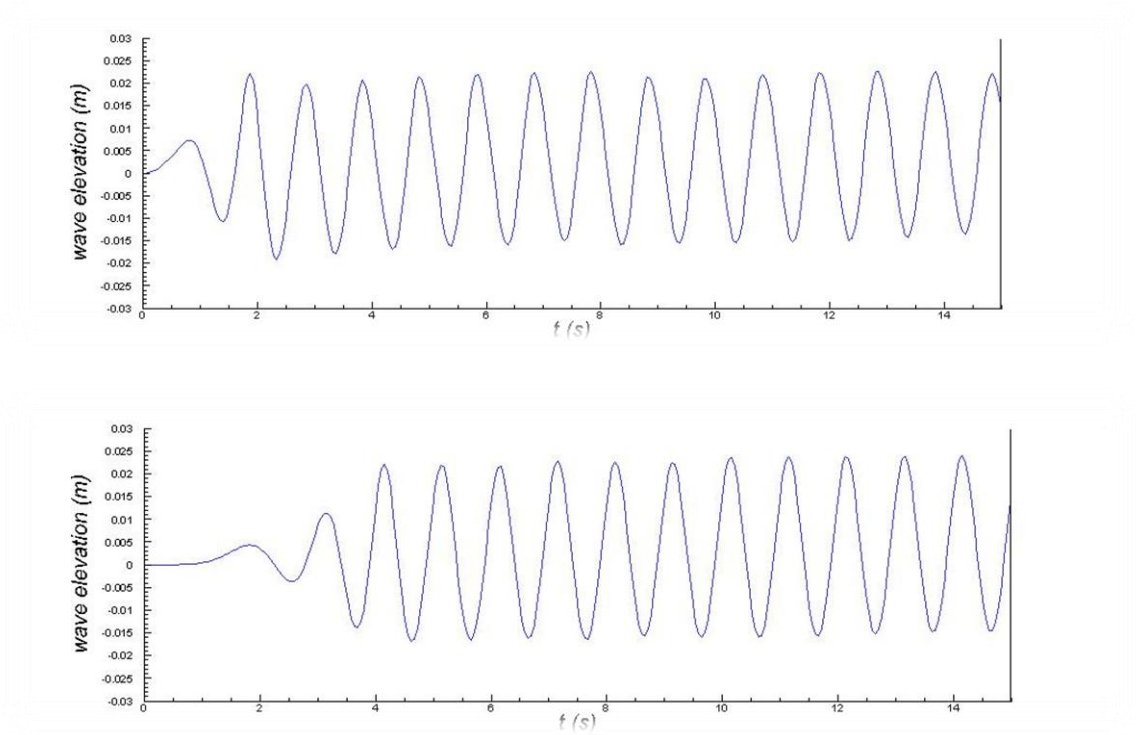

Fig. 4-6. Water surface time series for oblique waves of the incident angle $\theta = \pi$ at probes 1 and 3.

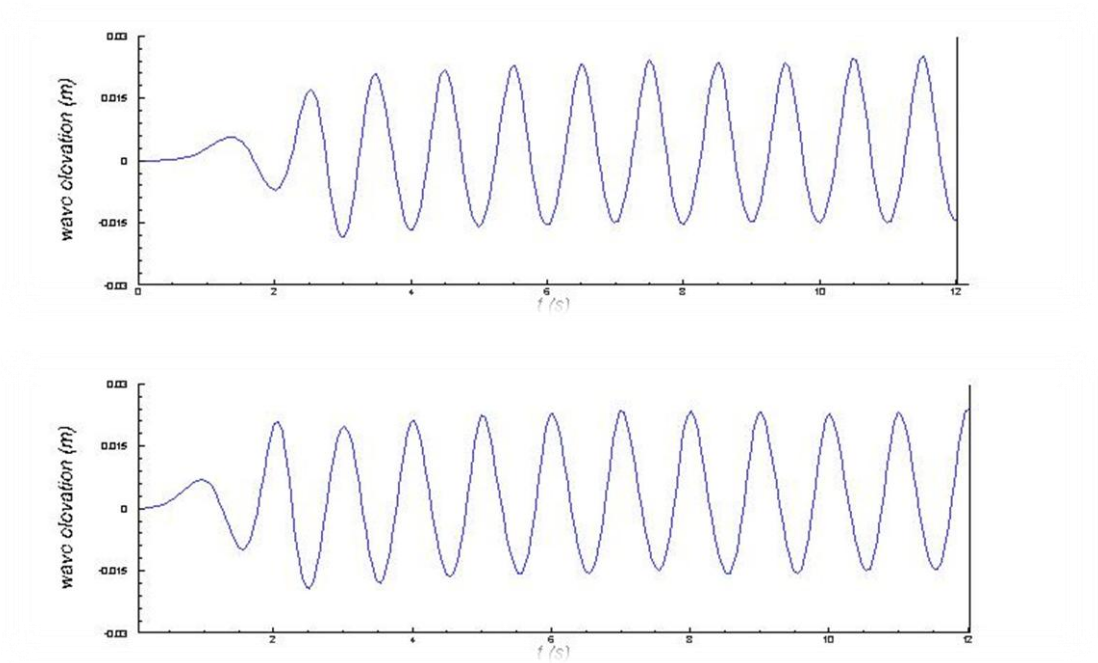

Fig. 4-7. Water surface time series for oblique waves of the incident angle $\theta = \pi$ in probes 1 and 3.

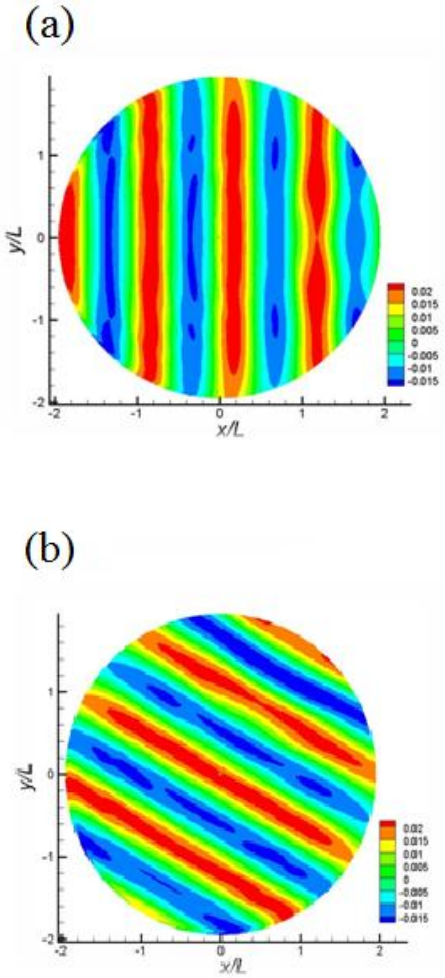

Fig. 4-8. Contour plot of instantaneous surface elevation of waves with

Incident angles (a) $\theta_i = \pi$, (b) $\theta_i = 4\pi/3$

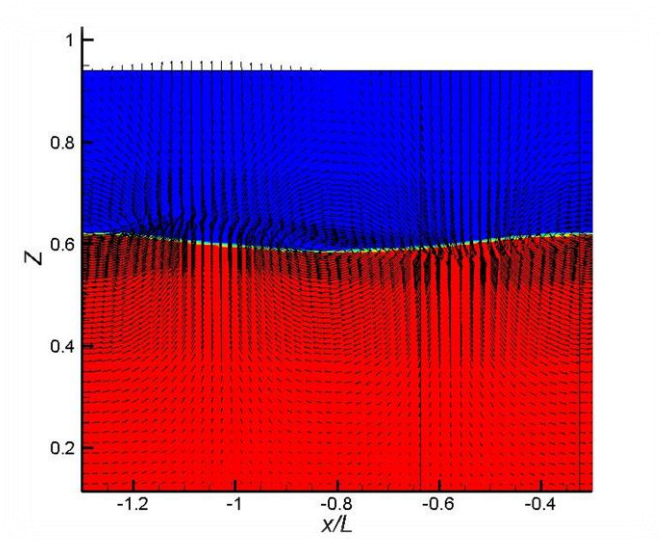

Fig. 4-9. Velocity field of slice *y/L*=0 at *t*=7.82 *s*.

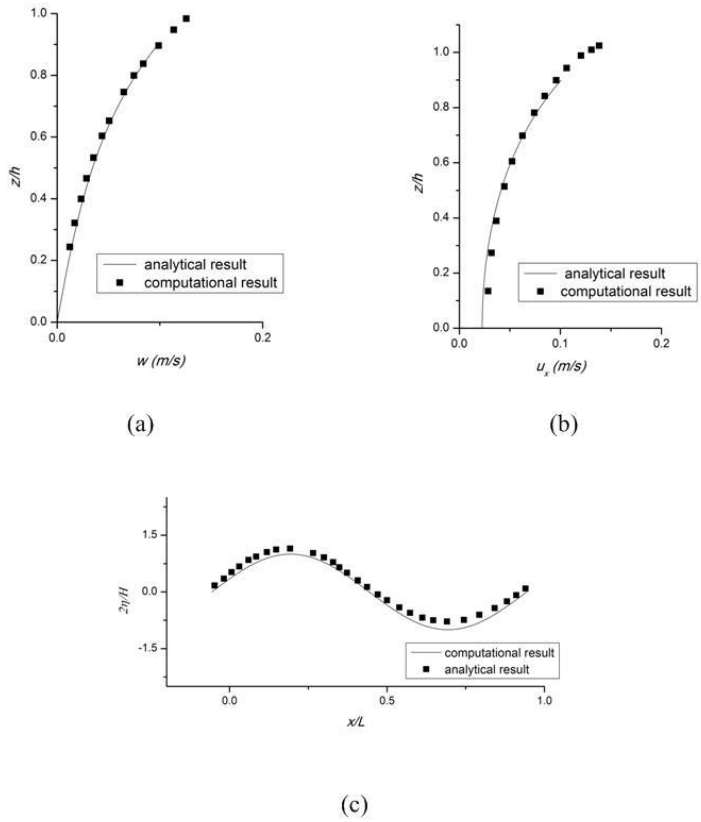

Fig. 4-10. Comparisons of vertical distributions of velocity components at section of *y/L*=0 between numerical result and linear wave theory: (a) vertical component at crest; (b) horizontal component at the middle of crest and trough, and (c) comparison of wave elevation normalized with incident wave height.

Results for the case $\theta_i = \pi$ can be compared with the theoretical two-dimensional results. Fig. 4-9 exhibits the velocity field at the slice $y = 0$. It can be seen from that figure that the velocities near the free surface are smoothed. And the vertical distribution at this slice can be compared with the theoretical results. Fig. 4-10(a) presents the comparisons of vertical velocity distributions in the section between the crest and the trough where the horizontal velocity component is zero between numerical results and linear wave theory. Comparisons of horizontal velocity distributions in the crest section where the vertical velocity component is zero are given in Fig. 4-10(b). Excellent agreement is observed between the two sets of results. In Fig. 4-10(c), the disagreements at the crest and tough in the comparison with the

linear wave theory profile are caused by the nonlinear effect.

4.3.2 Wave and cylinder interaction based on circular wave basin

The vertical cylinder is one of the most widely used structures in coastal and ocean area, and investigation of the wave interactions on the large volume is very important for the designs of coastal and ocean engineer. As a wave passes a vertical cylinder, its shape is affected by the presence of the cylinder. Wave diffraction around a vertical cylinder and wave force acting on the cylinder are the main topics in that research field.

Macamy and Fuchs (1954) based on first-order boundary value problem, derived the free surface elevation and wave force acting on the cylinder for finite depth water. Kriebel (1990) improved this problem to second order. With those methods, both the wave run-up and wave force can be computed from the derived equations. The results are normally treated to be the comparisons of numerical and experimental results. Numerical and experimental researches based on real time simulation of the wave-cylinder interaction are the other options for studying this problem. Galvin and Hallermeier (1955) studied the wave-up on a vertical cylinder with experimental data.

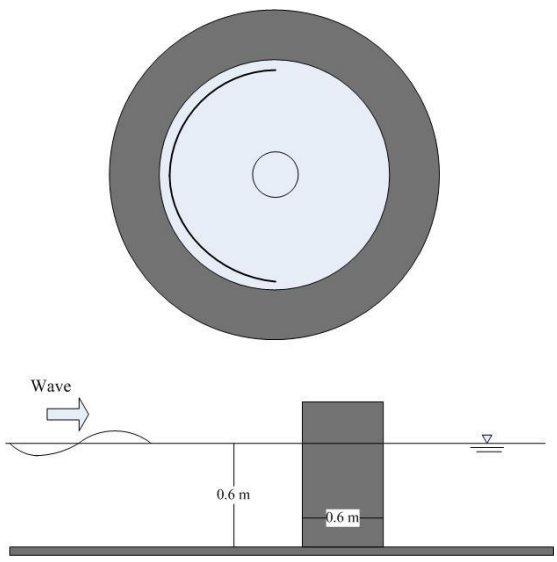

Fig. 4-11. Shape of vertical cylinder.

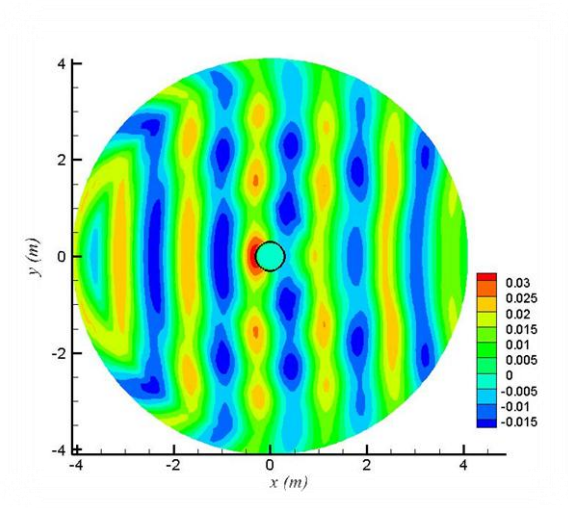

(a) t=10.4 s

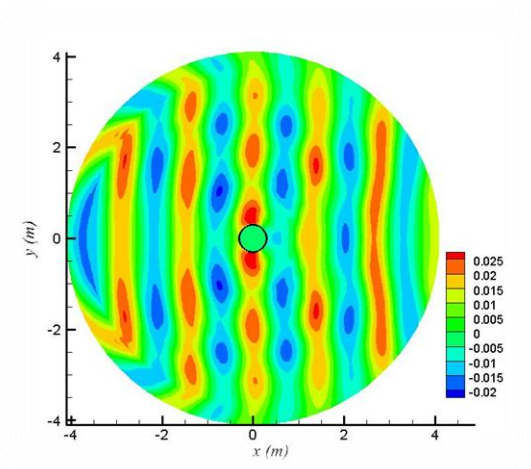

(b) t=10.6 s

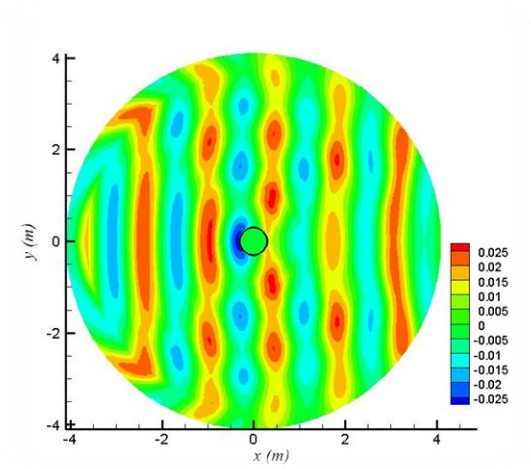

(c) t=10.9 s

Fig. 4-12. Time sequential wave elevation around a cylinder.

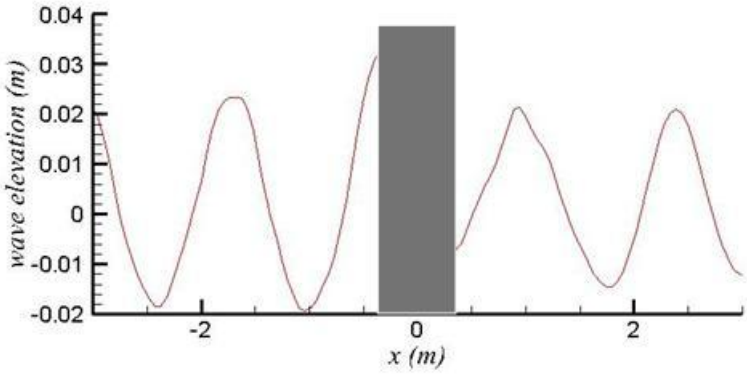

(a) t=10.4 s

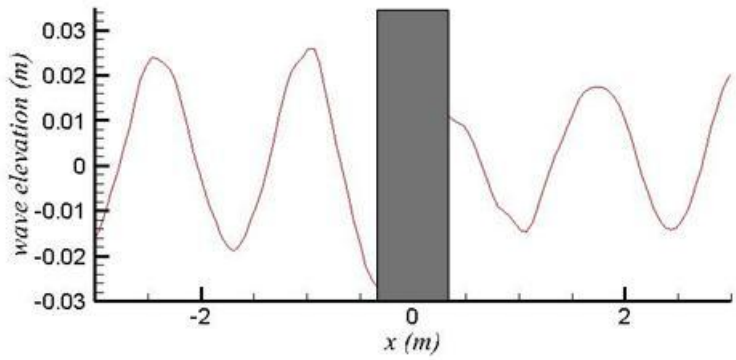

(b) t=10.9 s

Fig. 4-13. Time-sequential wave profiles along y=0.

To explain the circular wave basin model can be used to investigate oblique wave interactions with structure. Nonlinear wave interaction with an impermeable vertical cylinder is carried out with this numerical circular wave basin including the effects of fluid viscosity and fully nonlinear wave motions. The vertical cylinder is set in the middle of computation zone with a diameter D=0.6 m. Waves comes from $\theta_i = \pi$ direction and the wave height is 0.04 m, wave period is 0.98 s. Fig. 4-11 depicts the physical modeling that was used for the numerical prediction.

Figures in Fig 4-12 exhibit the instantaneous free surface elevations around the cylinder And in Fig. 4-13 show the time-sequential wave profiles along y=0. Fig.

4-12(a) shows the time when the maximum run-up achieved at the wind-side, and the wave profile along *y*=0 is shown in Fig 4-13(a). Fig 4-12(c) represents the snapshot of wave surface elevation when the minimum run-up achieved at the wind side and the wave profile along *y*=0 is shown in Fig. 4-13(b). As shown in Fig. 4-12, the wave crest lines in the entire domain are bended to the wind side. The wave height distribution normalized with the incident wave height shown in Fig. 4-14 is also blended to the wind side and that agrees with the studies of Kriebel (1999).

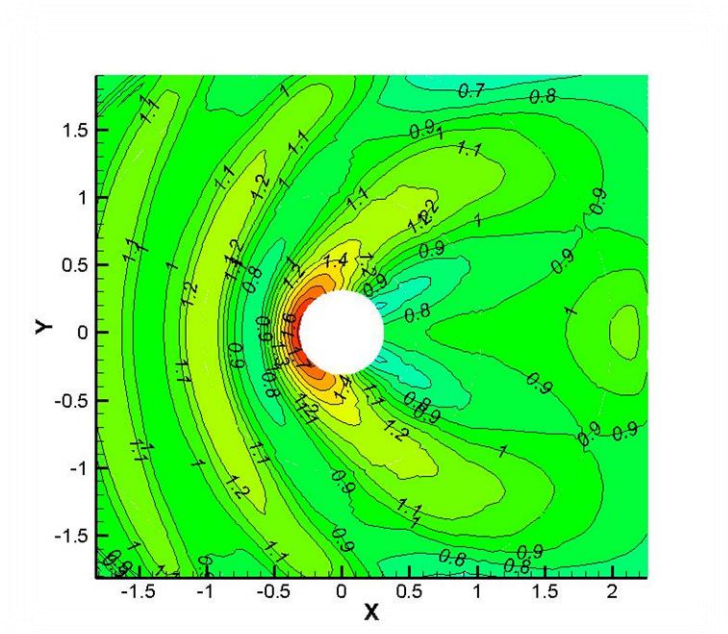

Fig. 4-14. Wave height distributions around a cylinder (unit: *m*).

4.4. Perspective of circular wave basin

The multi-directional waves are seen as the integration of oblique waves, so the present model is easy to extent to investigate multi-directional waves by submitting wave source functions calculated from Eq. (4-8). The wave source for multi-directional waves is formulated as:

$$Q(r_s,\theta_s,z,t)=\sum_i Q(r_s,\theta_{si},z,t)\,, \tag{4-10}$$

where $\theta_i-\frac{\pi}{2}\le\theta_{si}\le\theta_i+\frac{\pi}{2}$. Fig. 4-15 shows the computational result of two waves that integrate the oblique waves presented in Table 4-2, and the same computation

condition as the oblique wave simulations motioned above is used for the two crossing wave simulation. The wave crest lines can be described as rectangles in that figure, which agree with the properties of the interaction of two crossing waves.

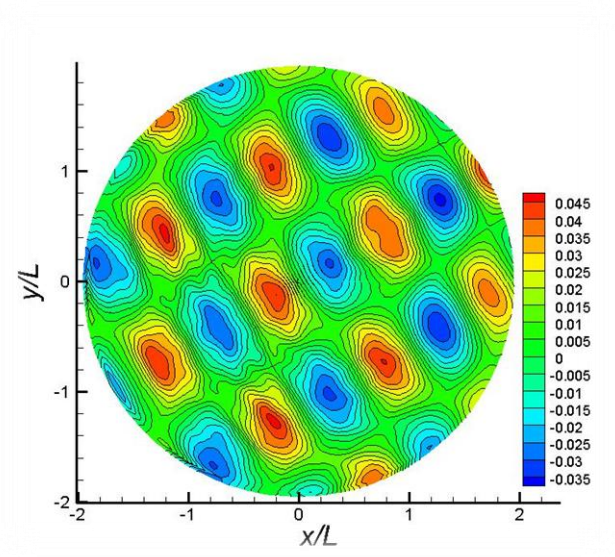

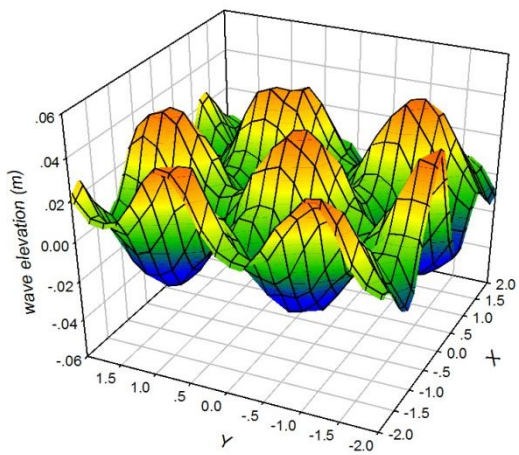

Fig. 4-15. Contour plot of instantaneous surface elevation of two crossing waves with incident angles: (a) $\theta_i = \pi$; (b) $\theta_i = 4\pi/3$ (unit: m).

4.5. Conclusions

As a result, a numerical solution was developed to investigate the generation and

propagation of the fully nonlinear oblique waves train on constant water depth.

Firstly, the viscous numerical circular wave basin simulation using the finite volume method based on Navier-Stokes equations in cylindrical coordinate was conducted to predict three dimensional wave motions.

Secondly, to demonstrate the advantages of this model, numerical simulations of oblique waves and two crossing waves were presented in this paper. The comparisons of vertical distributions of velocity components between computational results and linear wave theory were discussed. It was demonstrated that the present circular wave basin model can reliably reproduce the oblique waves propagating into the computational domain in any direction with large effective area. Thus, the current model can be used to simulate real sea waves and applied to analyze wave-structure interaction with waves coming from different directions. The wave-cylinder interaction was carried out as a case study of this model.

Finally, development of the present circular wave basin model to simulate two crossing waves was carried out to explain the ability of reproduction of multi-directional wave fields of the present model. Extension to multi-directional waves simulations will be our next application of the numerical wave basin in this research field.

References:

Hiraishi, T., Kanazawa, T. and Fujisaku, K., 1995. Development of multi-face directional random wave maker. Proceeding of 5th International Offshore and Polar Engineering Conference (ISOP), Hague, Netherlands.

Ito, K., Katsui, H.. Mochizuki, M. and Isobe, M., 1996. Non-reflected multi directional wave maker theory and experiments of verification. Proceeding of 25th International Conference of Coastal Engineering(ICCE), Orlando, Florida.

Kawasaki, K., 1999. Numerical simulation of breaking and post-breaking wave deformation process around a submerged breakwater. Coastal Engineering Journal 41, 201-223.

Kriebel, D. L., 1990. Nonlinear wave interaction with a vertical circular cylinder. Part I: diffraction theory. Ocean Engineering 17, 345-377.

Kriebel, D. L., 1992. Nonlinear wave interaction with a vertical circular cylinder. Part Π: wave run-up. Ocean Engineering 19, 75-99.

Larsen, J. and Dancy, H., 1983. Open boundaries in short waves simulation: a new approach. Coastal Engineering 7, 285-297.

Lin, P. Z. and Liu, P. L. F., 1999. Internal wave-maker for Navier-Stokes equations models. Journal of Water, Port coastal and Ocean Engineering 125, 207-215.

Lin P. Z. and Liu, P. L. F.,2004. Discussion of “vertical variation of the flow across the surf zone”. Costal Engineering 50, 161-164.

Lin P. Z. and Liu, P. L. F.,2004, Discussion of “vertical variation of the flow across the surf zone”. Costal Engineering 50, 161-164.

Maccamy, R. C. and Fuchs, R. A., 1954. Wave forces on piles: a diffraction theory. Technical memorandum, 69, US Army Coastal Engineering Research Center.

Park, J. C., Kim, M. H. et al., 2003. Fully nonlinear numerical wave tank (NWT) simulations and wave run-up prediction around 3-D structures. Ocean Engineering 30, 1969-1996.

Suh, Y. K., and Yeo, C. H., 2006. Finite volume method with zonal-embedded grids

for cylindrical coordinates. International Journal for Numerical Methods in Fluids 52, 263-295.

Tanaka, M., Ohyama, T. et al., 1994. Non-reflective multi-directional wave generation by source method. Proceedings of 24th Conference on Coastal Engineering, Kobe, Japan.

Williams, A. N. and Crull, W. W., 2000. Simulation of directional waves in a numerical basin by a desingularized integral equation approach. Ocean Engineering **27**, 603-624.

Chapter 5

Conclusions and perspective

One of main properties of the real ocean waves, which are the integration of irregular oblique waves, is the wave direction and challenges to study the real ocean waves with three-dimensional experimental and numerical rectangular wave basins are the wave refection from side walls and experimental structures and wave diffractions. Both the reflections waves that can be re-reflected by the paddles of serpent wave generator and wave diffractions depending on the incident wave angles affect the effective area of the wave basin. To circumvent this issue, in this study, a numerical circular wave basin was built, where the effect of the incident wave angles to the effective area can be neglected.

This wave basin model was developed based on the incompressible two-phase flow model, implemented by solving the Navier-Stokes equations in cylindrical coordinates with the volume of fluid method to track the free surface. In Chapter 2, the two-phase flow model was proposed by applying the projection method was used to solve the Navier-Stokes equations over the zonal embedded grids in cylindrical coordinates and

CICSAM-VOF based on the high resolution method to compute the volume fraction convection equation. The free surface tension was also considered with the Continuum Surface Force (CSF) method. Case studies of dam breakings in cylindrical tank were carried out based on this two-phase incompressible flow model to validate this model and results showed the perfect agreement with the properties of dam breaking.

In Chapter 4, the circular wave basin was successfully developed to generate oblique and multi-directional waves by applying the two-phase flow model introduced in Chapter 2 based on the concept of the circular wave basin. Waves were generated with a transparent wave source method implemented by adding a mass source to the continuity equation in a semi-circle wave source zone. The wave source zone was settled according to the incident wave angles to decrease the effect of the wave diffraction. Results of oblique waves showed that the effect of the wave incident angles to the effective area could be neglected and the effective area was only affected by the wave diffraction. The results of the oblique wave with an incident angle of π, showed the perfect agreements with that of the theoretical two-dimensional linear wave. The simulation of two crossing waves was carried out by integrating two oblique wave trains, which showed the present model can be able to extend to multi-directional waves simulations.

The present model can enlarge the effective area of three-dimensional wave basin in the application to oblique waves, for the effect of the wave re-reflection is avoided by the transparent wave generator and the diffraction effect is decreased by adjusting the wave source zone. Another advantage of this wave basin model is that the incident angle does not affect the effective area of the three-dimensional wave basin, which is

the limitation of the rectangular wave basins in application to oblique wave generations. Limitation of the proposed wave basin is that its performance in simulation of two-dimensional waves is not as good as that with rectangular wave basin, for wave diffraction cannot be avoided without side walls.

Based on the physical and numerical experiments, studies of the bridge failures due to tsunami were introduced in Chapter 3. Tsunami forces acting on bridges were used to analyze bridge failures. With cases categorized by the weight of bridges, the friction force effect in the process of bridge failure was analyzed and results in different cases showed that the vertical force played a very important role in the bridge failure problems. To simulate bridge in the present model, future study will be carried out to model a rectangular structure inside a circular tank.

Based on the circular wave basin, deeper researches will be done to analyze multi-directional waves in the future. Investigations of oblique wave-structures will be another topic to study the effect of the wave direction to structure, including the rectangular structures.

REN Xingyue

Doctoral Candidate, Nagoya University
Telephone: +8108043009417; **Email**: renxingyue@gmail.com
Anekusu 1C, Chikusa-ku, Nagoya, 464-0034, Japan

Education

- ✧ Doctor course in Civil Engineering (2009-present), Nagoya University
- ✧ Master of Port, Costal and Offshore Engineering (2006-2009), Ocean University of China
- ✧ Bachelor of Water and Wastewater Engineering (2002-2006), Jiangxi University of Science and Technology

Publications

Journal paper

1. Nakamura, T., Ren, X. Y., Morimoto, Y. and Mizutani, N., 2012. Numerical analysis of tsunami-induced wave force acting on a bridge deck and its effects on the motion of the bridge deck. Journal of JSCE, Series B3.
2. Nakamura, T., Mizutani, N, and Ren, X. Y., 2013. Numerical analysis of wave force acting on bridge deck due to tsunami and resulting motion of bridge deck. Journal of JSCE, Series A1.
3. Nakamura, T., Mizutani, N, and Ren, X. Y., 2013. Study on countermeasures for reducing tsunami force acting on a bridge superstructure and its effect on the motion of the superstructure. Journal of JSCE, Series B3.
4. Nakamura, T., Sawa, Y., Ren, X. Y., and Mizutani, N,2013. Experimental study on tsunami force acting on a bridge superstructure in critical condition. Journal of JSCE, Series B3.
5. Ren, X. Y., Mizutani, N, and Nakamura, T., Development of numerical circular wave basin based on two phase incompressible flow model. Submitted to Ocean Engineering.
6. Ren, X. Y., Mizutani, N, and Nakamura, T., Numerical investigation of wave forces on a vertical cylinder based on circular wave basin. Prepared (Chapter 4 of doctoral thesis).
7. Ren, X. Y., Mizutani, N, and Nakamura, T., Two phase incompressible flow model with embedded grid in cylindrical coordinate. Prepared (Chapter 2 of doctoral thesis).

Conference:

1. Ren, X. Y., Morimoto, Y., Nakamura, T., and Mizutani, N., 2011. Investigation of bridge failure caused by tsunami based on numerical method. JSCE Chubu Branch Annual Meeting 2011.